analytical chemistry

Letter

pubs.acs.org/ac

Coherent Anti-Stokes Raman Scattering Microspectroscopic Kinetic Study of Fast Hydrogen Bond Formation in Microfluidic Devices

Gennady V. Oshovsky,[†,‡,▽] Gianluca Rago,[‡,∥,§] James P. R. Day,[‡] Maarten L. Soudijn,[‡,⊥] William Rock,[∥] Sapun H. Parekh,[∥] Gianluca Ciancaleoni,[†,¶] Joost N. H. Reek,*[,†] and Mischa Bonn*[,‡,∥]

[†]Supramolecular and Homogeneous Catalysis, van't Hoff Institute for Molecular Sciences, University of Amsterdam, Science Park 904, 1098 XH Amsterdam, The Netherlands

[‡]Biosurface Spectroscopy Group, FOM Institute AMOLF, Science Park 104, 1098 XG Amsterdam, The Netherlands

[∥]Molecular Spectroscopy Department, Max Planck Institute for Polymer Research, Ackermannweg 10, 55128 Mainz, Germany

Supporting Information

ABSTRACT: The kinetics of a key noncovalent, hydrogen bonding interaction was studied in situ using coherent anti-stokes Raman scattering (CARS) microspectroscopy in a microfluidic device. The association of model compounds, pyridine and hexafluoroisopropanol, was quantitatively monitored with submicrometer resolution. Lower limits for the very high formation and dissociation rate constants of the model 1:1 pyridine−hexafluoroisopropanol hydrogen bonded complex in dichloromethane-d_2 were determined to be $k_1 > 10^5$ $M^{-1}s^{-1}$ and $k_{-1} > 333.3$ s^{-1}, respectively.

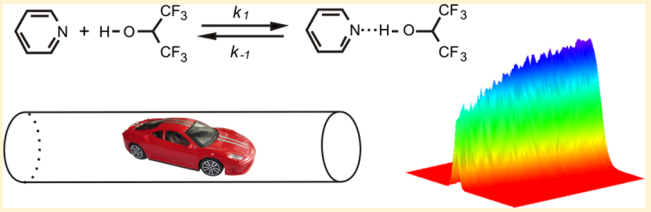

Hydrogen bonding is a fundamental noncovalent interaction that is key to many biological and supramolecular systems.[1−7] To understand the behavior of biomolecular[8,9] and related synthetic[6,10,11] complexes and systems[12,13] based on multiple H-bonds in more detail, including detailed formation and dissociation events of individual hydrogen bonds of the array, it is essential to develop technologies to study and understand the kinetic behavior of single hydrogen bonds in situ. Despite extensive studies on hydrogen bond interactions, known for almost a century,[14] determination of the rate of formation of single intermolecular H-bonds in the ground state has remained challenging.[1,2] Supramolecular kinetics[15−19] of single intermolecular hydrogen bonds have been broadly addressed for systems containing excited state species,[20] formed with the help of (advanced) laser techniques. Ground state studies have largely focused on two and more H-bond assemblies.[6,10,21] The key challenge of studying ground state single intermolecular H-bond formation is the typically low activation energy barrier for the formation of a hydrogen bond. In addition, the presence of several competing processes acting on comparable time scales, such as predissociation of noncovalent aggregates of reacting species and competitive complex formation with solvent molecules (e.g., water),[7,22−25] are complicating such studies. Moreover, hydrogen bonding generally requires opening and rearrangement of a solvation shell, and these solvent molecules are often interacting with the polar groups participating in hydrogen bonding.[26,27]

The existing methods to study very fast interactions, such as temperature jump, ultrasonic relaxation, and photophysical methods, are invasive in nature.[18] They put energy into a supramolecular system to bring its components to the excited state or to push it out-of-the equilibrium and hence destroy its components' solvates and noncovalent aggregates. However, these species are essential for the real solution, since they influence the formation rate of noncovalent complexes, and therefore, the above-mentioned methods provide an idealized kinetic picture. It would therefore be of interest to develop analytic tools that allow one to monitor these supramolecular events in a noninvasive manner to get a more detailed understanding of the solution processes.[28] This is especially important in view of the significant differences in the formation rates of different types of simple supramolecular components obtained by the above-mentioned "invasive" methods (>10^6 $M^{-1}s^{-1}$)[21,29−31] in comparison with electrochemical and gravimetric tools (<10 $M^{-1}s^{-1}$).[32,33] Here, we show that quantitative coherent anti-stokes Raman scattering (CARS) microspectroscopy,[34−40] a label-free imaging technique used in a microfluidic device,[41] is an interesting platform to interrogate H-bond kinetics without strong influence of the measuring technique on the interaction. This is achieved by the excitation of submicrometer areas of steadily flowing species in the course of CARS measurements, which does not influence the overall interaction behavior. It has been shown to be capable of studying fast chemical processes ($k_1 > 300$ $M^{-1}s^{-1}$) with high sensitivity and good temporal, spatial, and spectral resolution when combined with a simple microfluidic device.[42] In this study, we apply CARS microspectroscopy to determine the kinetics of formation of a well-defined single intermolecular H-bond.

Received: July 19, 2013
Accepted: August 28, 2013

   dx.doi.org/10.1021/ac402233n | *Anal. Chem.* XXXX, XXX, XXX−XXX

We study pyridine as a model hydrogen bond acceptor (**1** in Scheme 1), since hydrogen bonding to pyridine nitrogen atom is an essential pattern in DNA base pairing and it occurs in many natural and synthetic receptors systems, self-assemblies, and supramolecular polymers. Hexafluoroisopropanol (HFIP, **2** in Scheme 1) is chosen as a strong hydrogen bond donor.[43] This combination provides a substantial amount of the singly H-bonded complex (**3** in Scheme 1) with association constant (K_a) = 300 M^{-1} (in polar aprotic dichloromethane-d_2, as determined by ^{19}F NMR titration studies).

Hydrogen bond formation with the pyridine nitrogen atom is readily observed with Raman spectroscopy.[44,45] A titration of pyridine (**1** in Scheme 1), in which concentration is kept constant (0.5 M) at every titration point, with increasing amounts of hexafluoroisopropanol (**2** in Scheme 1) results in significant changes in the pyridine ring breathing vibrations (−987.9 cm^{-1}) and a shift in its triangle vibrations (−1026.0 cm^{-1}). Specifically, Figure 1 shows the MEM-retrieved Im[$\chi^{(3)}$] CARS signal, which is equivalent to the Raman signal.[46−48] Hexafluoroisopropanol **2** itself does not have signals in the measured area, and the solvent signal appears at −1046.3 cm^{-1}. It is apparent that the free pyridine mode at −987.9 cm^{-1} decreases and eventually disappears with increasing concentration of binding partner **2**. Simultaneously, a new signal at −1001.5 cm^{-1} appears. The moderate difference of 13.6 cm^{-1} between the positions of these two signals confirms that the new signal corresponds to H-bonded complex **3**, rather than to protonated pyridine $C_5H_5NH^+$ for which the signal is shifted by ∼30 cm^{-1} (until around −1018 cm^{-1}) in comparison with free pyridine **1**.[45] The changes in the ring breathing mode of the pyridine ring were used to follow and to quantify the concentration changes of the reacting species in the microfluidic device.

Scheme 1. Model Hydrogen-Bonded Complex 3 Formation between Pyridine 1 and Hexafluoroisopropanol 2

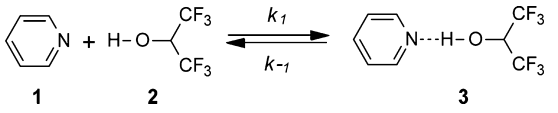

1 2 3

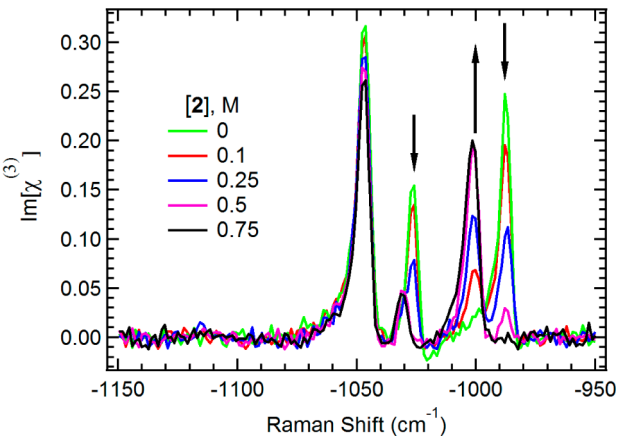

Figure 1. CARS titration data ([**1**] = 0.5 M). With increasing concentration of **2**, the free mode at −987.9 cm^{-1} decreases as a new signal at −1001.5 cm^{-1} appears, attributed to **3**.

The CARS kinetic measurements are carried out in an Y-shaped microfluidic device. Two 500 mM solutions in dichloromethane-d_2 (pyridine **1** from one side and HFIP **2** from the other) are injected into the microfluidic device under laminar flow conditions (Figure 2a). CARS spectra are obtained with a spatial resolution of 0.5 × 0.5 × 1 μm ($x \times y \times z$) at fixed depth (z = 20 μm) in the center of the channel in 1 μm steps in

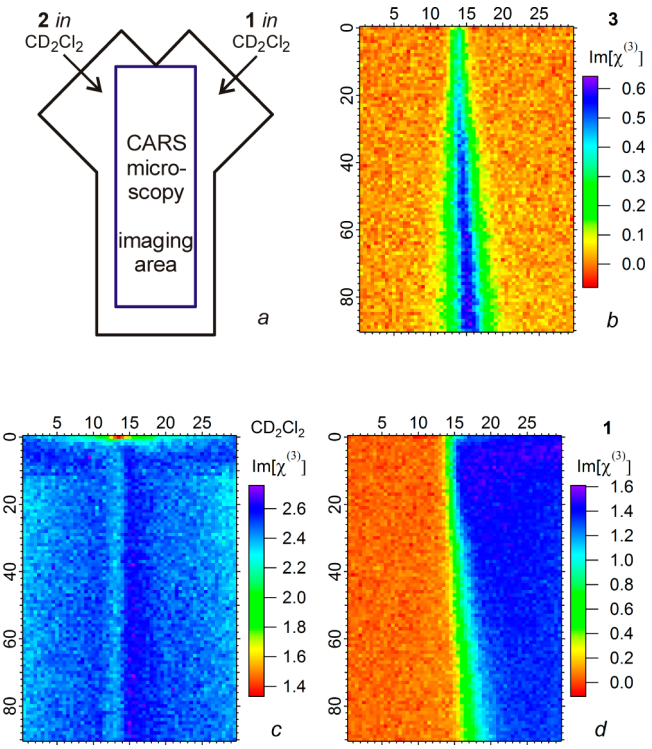

Figure 2. Schematic presentation of the experimental setup (a), CARS microscopic images of the appearance of complex **3** (b), variability of the solvent signal intensity (c), and the disappearance of reagent **1** (d).

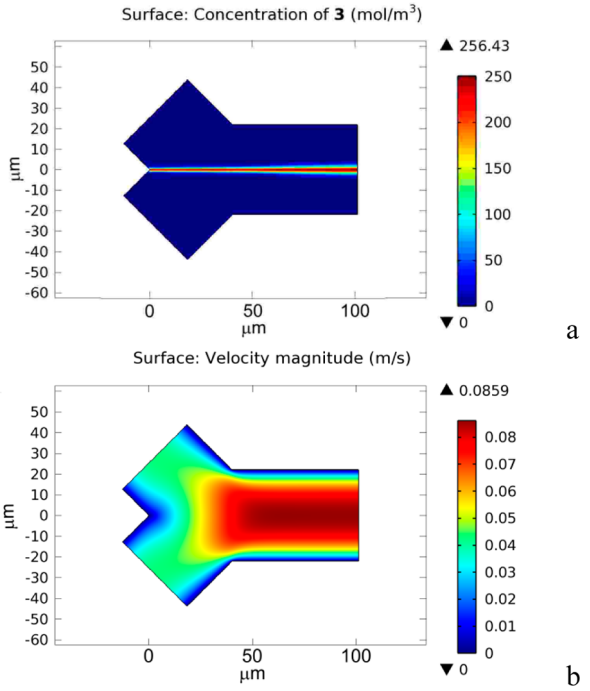

Figure 3. COMSOL modeled: progress of the reaction in the microchannel, an example for $k_1 = 10^6$ $M^{-1}s^{-1}$ (a); change of the flow rate across the microchannel (b).

dx.doi.org/10.1021/ac402233n | Anal. Chem. XXXX, XXX, XXX−XXX

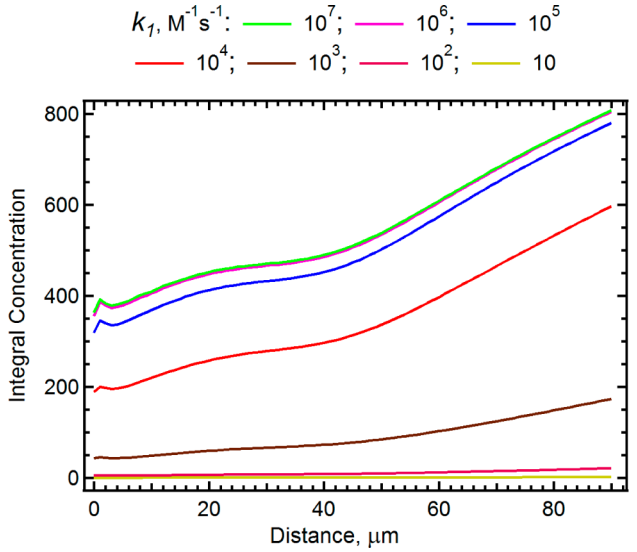

Figure 4. Progress of the reaction in microchannel, depending on the reaction rate (k_1, $M^{-1}s^{-1}$).

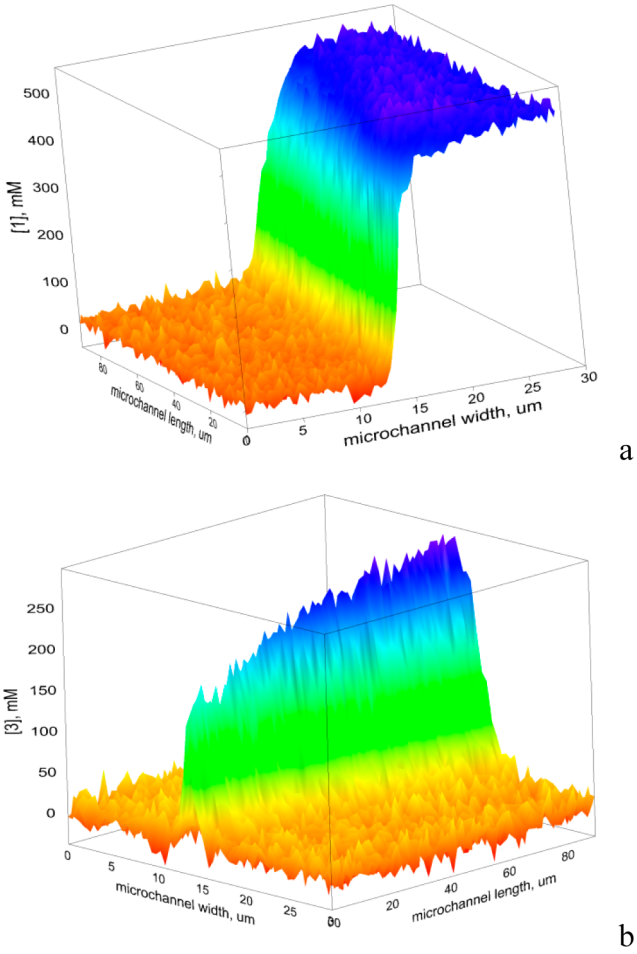

Figure 5. The progress of the reaction in the microchannel (3D view).

the direction of the flow and 0.5 μm steps perpendicularly to the flow over a horizontal rectangular area of 30 × 90 μm (5400 spectra, Figure 2a). Integration of the signals of complex **3**, solvent, and pyridine **1** in MEM-processed CARS spectra[46−48] resulted in the images presenting the evolution of complex **3**, the change of the molar fraction of the solvent upon mixing the

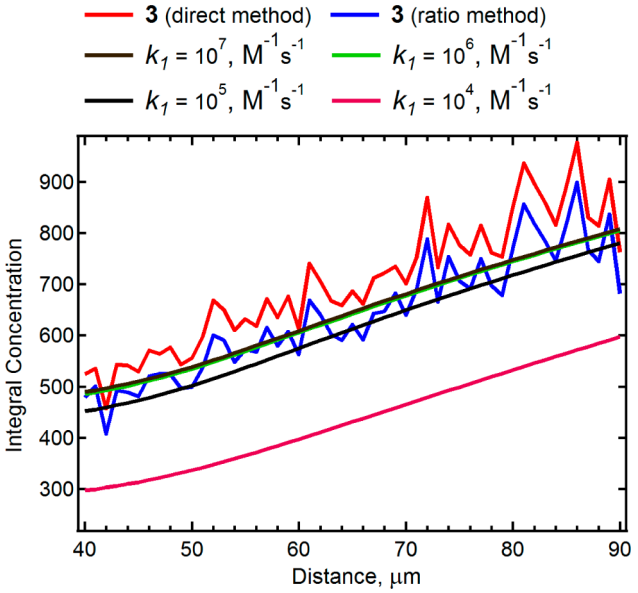

Figure 6. Experimental (blue and red curves) and computational integrated data of the complexation progress across the microchannel.

solutions, and the consumption of the initial reagent **1** in the course of the complexation process (Figure 2b−d, respectively).

We model the diffusion-reaction behavior of two reactants and product in the microchannels (Figure 3a) to extract quantitative information on reaction rates. The COMSOL Multiphyiscs package was used to build a lattice-based model of the fluidic processes using diffusion coefficients for each reactant (and solvent) determined using diffusion PGSE (pulsed-field gradient spin echo) NMR experiments. The diffusion coefficients of pyridine **1**, hexafluoroisopropanol **2**, and complex **3** were determined in dichloromethane-d_2 as 2.95 × 10^{-9}, 2.68 × 10^{-9}, and 1.91 × 10^{-9} m^2s^{-1}, respectively (details are given in the Supporting Information).[49,50] The model takes into account the rather complicated flow-profile, especially at the microfluidic Y-junction (Figure 3b). A comparison of Figure 3a with Figure 2b shows qualitative agreement between the host−guest complex appearance measured with CARS and that predicted with the simple model, shown here for k_1 = 10^6 $M^{-1}s^{-1}$.

To determine the kinetics of host−guest complex formation, it is helpful to consider the host−guest complex **3** concentration as a function of time (or, equivalently, position along the length of the channel; position 0 is the initial mixing point of **1** and **2**). This is accomplished by integrating the signal in Figure 2b across the channel width at each position along the length of the channel. Figure 4 shows these reaction profiles for the computational model. The family of curves shown result from varying the H-bond formation rate constant (k_1), assuming a singular rate constant for this process, from ∼10 M^{-1} s^{-1} < k_1 < 10^6 $M^{-1}s^{-1}$. The rate of the reaction increases after ∼45 μm, which is due to significant increase in the flow rate across the channel after the Y-junction (see Figure 3b).

To compare these results with the experimental data from CARS, a calibration is necessary to convert CARS intensities into absolute concentrations. The calibration was carried out with four solutions of known chemical composition (based on 1:1 complexation model equilibrium and its steady state binding constant). CARS measurements of 100 spectra of

dx.doi.org/10.1021/ac402233n | Anal. Chem. XXXX, XXX, XXX−XXX

identical chemical composition were measured in a lab-on-a-chip for every solution (see Supporting Information). In the calibration, we used both the absolute signal intensity $\mathrm{Im}[\chi^{(3)}]$ (a direct method) and the ratio of the measured signal intensity $\mathrm{Im}[\chi^{(3)}]$ to that of a reference (solvent, CD_2Cl_2) (a ratio method). The use of a reference signal allows for straightforward correction of laser intensity fluctuations and variations over the relatively long measurement time (~3−5 h) and for chip effects. Higher values for the concentrations of complex **3** were obtained by simply using the absolute signal intensity $\mathrm{Im}[\chi^{(3)}]$ (see the Supporting Information for details).

The calibration procedure thus allows the visualization of the local concentrations of reactants and the product in the microfluidic device in the course of the progress toward hydrogen bonding equilibrium. The results are shown for pyridine **1** and the product complex **3** in Figure 5a,b, respectively. Integration of the product yield was performed by fitting Gaussian profiles to cuts orthogonal to the direction of the flow.

The comparison of the experimental results with that obtained by modeling (Figure 6) provides a lower limit for the formation rate constant of the complex **3**, i.e., $k_1 > 10^5$ $M^{-1}s^{-1}$, and the dissociation constant is $k_{-1} > 333.3$ s^{-1}, given that $K_a = 300$ M^{-1} for the solvent. While our results have not allowed the identification of the exact values of the rate constants yet, we note that the CARS-based method combined with microfluidics provides a unique data set that is not possible with any other method.

In conclusion, we use label-free vibrational microscopy to explicitly measure the kinetics of the formation of a single hydrogen bond via intermolecular interaction in a real, nonideal system. Our results demonstrate that the formation rate constant for pyridine−hexafluoroisopropanol complex **3** is $k_1 > 10^5$ $M^{-1}s^{-1}$ and the dissociation constant is $k_{-1} > 333$ s^{-1}. The label-free and microscopic nature of CARS imaging combined with simple microfluidic devices is a powerful tool to study (bio)supramolecular kinetics in situ. We envision that further improvements of the sensitivity and precision (and with that the time resolution) of this technique will allow one to distinguish fast microscopic steps in more complex (bio)-molecular complexation and self-assembly processes including solvent effects in real time.

■ ASSOCIATED CONTENT

Ⓢ Supporting Information

Full experimental details, COMSOL models, data analysis. This material is available free of charge via the Internet at http://pubs.acs.org.

■ AUTHOR INFORMATION

Corresponding Authors

*E-mail: j.n.h.reek@uva.nl.
*E-mail: bonn@mpip-mainz.mpg.de.

Present Addresses

▽G.V.O.: Department of Chemistry and Life Sciences, Inholland University of Applied Sciences, De Boelelaan 1109, 1081 HV Amsterdam, The Netherlands.
⊥M.L.S.: Quantum Gases and Quantum Information group, van der Waals-Zeeman Institute, Institute of Physics, University of Amsterdam, Science Park 904, 1098 XH Amsterdam, The Netherlands.
¶G.C.: Istituto di Scienze e Tecnologie Molecolari del CNR (CNR-ISTM), c/o Dipartimento di Chimica, Università degli Studi di Perugia, I-06123 Perugia, Italy.
§G.R.: Deloitte Consulting B.V., Laan van Kronenburg 2, 1183 AS, Amstelveen, The Netherlands.

Notes

The authors declare no competing financial interest.

■ ACKNOWLEDGMENTS

The authors are grateful to Dr. Guillaume Berthon-Gelloz for fruitful discussions that inspired this research. This work was supported by the Council for Chemical Sciences of The Netherlands Organization for Scientific Research (CW-NWO) and Max Planck Institute for Polymer Research.

■ REFERENCES

(1) Leszczynski, J. In *Hydrogen Bonding - New Insights*; Grabowski, S. J., Ed.; Series: Challenges and Advances in Computational Chemistry and Physics; Springer: New York, 2006.
(2) Desiraju, G. R.; Steiner, T. *The Weak Hydrogen Bond in Structural Chemistry and Biology*; Oxford University Press Inc.: New York, 1999.
(3) Reedijk, J. *Chem. Soc. Rev.* **2013**, *42*, 1776−1783.
(4) Grabowski, S. J. *Chem. Rev.* **2011**, *111*, 2597−2625.
(5) Steiner, T. *Angew. Chem., Int. Ed.* **2002**, *41*, 48−76.
(6) Prins, L. J.; Reinhoudt, D. N.; Timmerman, P. *Angew. Chem., Int. Ed.* **2001**, *40*, 2382−2426.
(7) Marechal, Y. *The Hydrogen Bond and the Water Molecule. The Physics and Chemistry of Water, Aqueous and Bio-Media*; Elsevier: Boston, 2007.
(8) Kool, E. T.; Morales, J. C.; Guckian, K. M. *Angew. Chem., Int. Ed.* **2000**, *39*, 990−1009.
(9) Zhou, H.-X.; Pang, X.; Lu, C. *Phys. Chem. Chem. Phys.* **2012**, *14*, 10466−10476.
(10) de Greef, T. F. A.; Ligthart, G. B. W. L.; Lutz, M.; Spek, A. L.; Meijer, E. W.; Sijbesma, R. P. *J. Am. Chem. Soc.* **2008**, *130*, 5479−5486.
(11) Schneider, H.-J. *Angew. Chem., Int. Ed.* **2009**, *48*, 3924−3977.
(12) Lehn, J.-M. *Angew. Chem., Int. Ed.* **2013**, *52*, 2836−2850.
(13) Li, J.; Nowak, P.; Otto, S. *J. Am. Chem. Soc.* **2013**, *135*, 9222−9239.
(14) Latimer, W. M.; Rodebuch, W. H. *J. Am. Chem. Soc.* **1920**, *42*, 1419−1433.
(15) Rieth, S.; Hermann, K.; Wang, B.-Y.; Badjić, J. D. *Chem. Soc. Rev.* **2011**, *40*, 1609−1622.
(16) Nau, W. M.; Wang, X. *ChemPhysChem* **2002**, *3*, 393−398.
(17) Izatt, R. M.; Pawlak, K.; Bradshaw, J. S. *Chem. Rev.* **1995**, *95*, 2529−2586.
(18) Bohne, C. *Langmuir* **2006**, *22*, 9100−9111.
(19) Izatt, R. M.; Pawlak, K.; Bradshaw, J. S.; Bruening, R. L. *Chem. Rev.* **1991**, *91*, 1721−2085.
(20) Han, K.-L.; Zhao, G.-J., Eds. *Hydrogen Bonding and Transfer in the Excited State*; John Wiley & Sons: Hoboken, NJ, 2010.
(21) Hammes, G. G.; Park, A. C. *J. Am. Chem. Soc.* **1969**, *91*, 956−961.
(22) Rehm, T. H.; Schmuck, C. *Chem. Soc. Rev.* **2010**, *39*, 3597−3611.
(23) Kubik, S. *Chem. Soc. Rev.* **2010**, *39*, 3648−3663.
(24) Oshovsky, G. V.; Reinhoudt, D. N.; Verboom, W. *Angew. Chem., Int. Ed.* **2007**, *46*, 2366−2393.
(25) Laughrey, Z.; Gibb, B. C. *Chem. Soc. Rev.* **2011**, *40*, 363−386.
(26) Tielrooij, K. J.; Garcia-Araez, N.; Bonn, M.; J., B. H. *Science* **2010**, *328*, 1006−1009.
(27) Bhattacharyya, K. *Acc. Chem. Res.* **2003**, *32*, 95−101.
(28) Lehn, J. M. *Science* **2002**, *295*, 2400−2403.
(29) Franchi, P.; Lucarini, M.; Pedulli, G. F.; Sciotto, D. *Angew. Chem., Int. Ed.* **2000**, *39*, 263−266.
(30) Yasunaga, T.; Nishikawa, S.; Tatsumoto, N. *Bull. Chem. Soc. Jpn.* **1971**, *44*, 2308−2312.

(31) Zhang, X. Y.; Gramlich, G.; Wang, X. J.; Nau, W. M. *J. Am. Chem. Soc.* **2002**, *124*, 254−263.
(32) Mohammad, M.; Rauf, A.; Rauf, S.; Tariq, M. *J. Phys. Org. Chem.* **2012**, *25*, 1269−1274.
(33) Ebara, Y.; Itakura, K.; Okahata, Y. *Lagmuir* **1996**, *12*, 5165−5170.
(34) Day, J. P. R.; Domke, K. F.; Rago, G.; Kano, H.; Hamaguchi, H.-o.; Vartiainen, E. M.; Bonn, M. *J. Phys. Chem. B* **2011**, *115*, 7713−7725.
(35) Roy, S.; Gord, J. R.; Patnaik, A. K. *Prog. Energy Combust.* **2010**, *36*, 280−306.
(36) Evans, C. L.; Xie, X. S. *Ann. Rev. Anal. Chem.* **2008**, *1*, 883−909.
(37) Müller, M.; Zumbusch, A. *ChemPhysChem* **2007**, *8*, 2156−2170.
(38) Cheng, J. X.; Xie, X. S. *J. Phys. Chem. B* **2004**, *108*, 827−840.
(39) Volkmer, A. *J. Phys. D* **2005**, *38*, R59−R81.
(40) Lee, Y. J.; Moon, D.; Migler, K. B.; Cicerone, M. T. *Anal. Chem.* **2011**, *83*, 2733−2739.
(41) Salieb-Beugelaar, G. B.; Simone, G.; Arora, A.; Philippi, A.; Manz, A. *Anal. Chem.* **2010**, *82*, 4848−4864.
(42) Schafer, D.; Squier, J. A.; van Maarseveen, J.; Bonn, D.; Bonn, M.; Müller, M. *J. Am. Chem. Soc.* **2008**, *130*, 11592−11593.
(43) Hunter, C. A. *Angew. Chem., Int. Ed.* **2004**, *43*, 5310−5324.
(44) Berg, E. R.; Freeman, S. A.; Green, D. D.; Ulness, D. J. *J. Phys. Chem. A* **2006**, *110*, 13434−13446.
(45) Berg, E. R.; Green, D. D.; Diane, C.; Moliva, A.; Bjerke, B. T.; Gealy, M. W.; Ulness, D. J. *J. Phys. Chem. A* **2008**, *112*, 833−838.
(46) Cicerone, M. T.; Aamer, K. A.; Lee, Y. J.; Vartiainen, E. *J. Raman Spectrosc.* **2012**, *43*, 637−643.
(47) Vartiainen, E. M.; Rinia, H. A.; Müller, M.; Bonn, M. *Opt. Express* **2006**, *14*, 3622−3630.
(48) Rinia, H. A.; Bonn, M.; Müller, M.; Vartiainen, E. M. *ChemPhysChem* **2007**, *8*, 279−287.
(49) Cohen, Y.; Avram, L.; Frish, L. *Angew. Chem., Int. Ed.* **2005**, *44*, 520−554.
(50) Macchioni, A.; Ciancaleoni, G.; Zuccaccia, C.; Zuccaccia, D. *Chem. Soc. Rev.* **2008**, *37*, 479−489.

Supporting Information

CARS Microspectroscopic Kinetic Study of Fast Hydrogen Bond Formation in Microfluidic Devices

Gennady V. Oshovsky,[†,‡] Gianluca Rago,[‡,∥,§] James P. R. Day,[‡] Maarten L. Soudijn,[‡] William Rock,[∥] Sapun H. Parekh,[∥] Gianluca Ciancaleoni,[†] Joost N. H. Reek,*[,†] and Mischa Bonn*[,‡,∥]

[†] Supramolecular and Homogeneous Catalysis, van 't Hoff Institute for Molecular Sciences, University of Amsterdam, Science Park 904, 1098 XH Amsterdam, The Netherlands

[‡] Biosurface Spectroscopy Group, FOM Institute AMOLF, Science Park 104, 1098 XG Amsterdam, The Netherlands

[∥] Molecular Spectroscopy Department, Max Planck Institute for Polymer Research, Ackermannweg 10, 55128 Mainz, Germany

[§] Deloitte Consulting B.V., Laan van Kronenburg 2, 1183 AS Amstelveen, The Netherlands

* j.n.h.reek@uva.nl (J.N.H.R.), bonn@mpip-mainz.mpg.de (M.B.)

Contents

1. General Information

CARS measurements were performed in a well ventilated dark room. In the course of the CARS measurements the use of a gas mask IS OBLIGATORY due to the toxicity of the chemicals used in the course of experiments. Pyridine was bought from Aldrich Chemical and dried by a two step procedure: boiling above NaOH pellets followed by distillation, and boiling over P_2O_5 followed by distillation under dry nitrogen. Hexafluoroisopropanol was bought from Aldrich Chemical, and extra dry dichloromethane-d_2 from Cortecnet; these are used as it is. Y-shaped microfluidic devices are bought from Micronit Microfluidics. NMR measurements were performed using NMR Varian Mercury-VX (300 MHz) and Bruker DRX300 (300 MHz).

CARS setup:[1] A dual-output laser source (Leukos-CARS, Leukos, Limoges, France) provides the pump and Stokes beams. The source is a passively Q-switched 1064-nm microchip laser, delivering < 1-ns pulses at 32 kHz repetition rate and ~300 mW average power. The laser beam is equally divided into two parts with a beam splitter. One part is sent through a bandpass filter (FL1064-10, Thorlabs) and used directly as the pump beam. The other part is introduced into a photonic crystal fiber that creates supercontinuum emission from 420–2400 nm at the fiber output, with > 100 μW nm^{-1} spectral power density from 1.05 μm to 1.6 μm. The supercontinuum is coupled out of the fiber with a reflective collimator (RC04APC-P01, Thorlabs) and passed through 700-nm (FEL0700, Thorlabs) and 830-nm (LP02-830RS-25, Semrock) longpass filters. The Stokes and pump beams are overlapped at a dichroic mirror (LP02-1064RU-25, Semrock) and introduced into a modified inverted microscope (Eclipse Ti-U, Nikon). The pump and Stokes pulses are tightly focused onto the sample with a near IR objective (PE IR Plan Apo 100X, NA 0.75, Seiwa). The sample is mounted on nested stepper-motor driven (Microstage, Mad City Labs) and piezo driven stages (Nano-PDQ 375 HS, Mad City Labs), shown in Figure s1, that together provide 25 mm travel range with < 1-nm resolution. The CARS signal generated by the sample is collected in the forward direction by another objective (M-20X, NA 0.4, Newport) and sent through notch (NF03-532/1064E-25, Semrock) and short-pass filters (FES1000, Thorlabs) to remove the pump and Stokes beams. The filtered CARS beam is dispersed by a spectrometer (Shamrock 303i, 300 lines mm^{-1}, 1000-nm blaze, Andor) and detected on a deep-depletion CCD (Newton DU920P-BR-DD, Andor). The sample is raster scanned across the focal volume with x×y steps

of 0.5×1 µm in plane. Due to the large dimensions of the area to investigate, twodimensional images are reconstructed from consecutive tiles with in plane dimensions of 15×30 µm. For each position in the sample, a CARS spectrum in the range between -3400 and -600 cm^{-1} is acquired. CARS images were acquired with pixel dwell times of 1s.

The chip itself was placed in a custom made holder (Figure s2) and mounted on a the piezo-driven stage (Figure s1). Two solutions of interacting components (both 0.5 M in dichloromethane-d_2) were injected to the microfluidics device from 0.25 or 0.5 mL hamiltonian syringes via capillaries. The stable injection rate (2 µL/min) is achieved by the use of Harvard 22 syringe pump (Harvard Apparatus) with the standard 2-syringe rack. The temperature of the measurements is 18 °C.

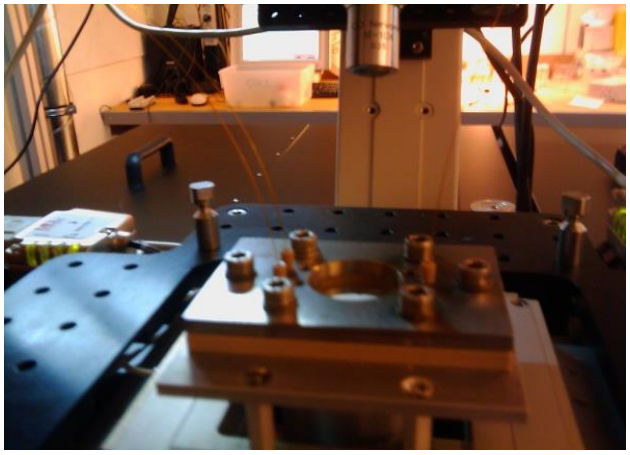

Figure s1. The chip in the chip holder mounted on a piezo-driven stage.

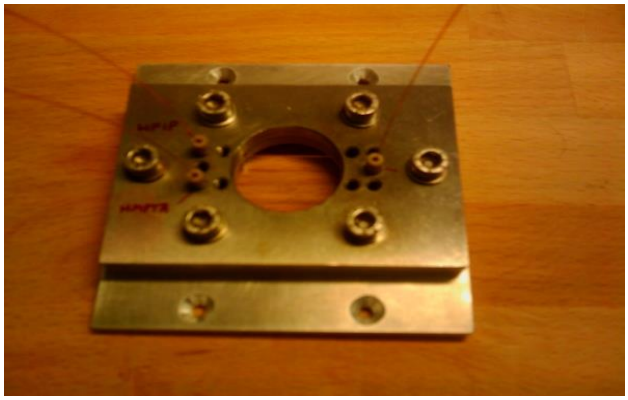

Figure s2. The lab-on-a-chip in a chip holder

CARS data analysis was performed with Igor Pro (version 6.2.2.2).

2. CARS Spectra

The components of the model equilibrium (Scheme s1), spectra of the interacting components pyridine **1**, hexafluoroisopropanol **2** and the complex **3** (as a dominant component in the equilibrium), are shown in Figures s3, s4, and s5.

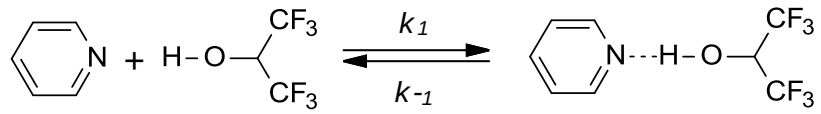

1 **2** **3**

Scheme s1. The studied equilibrium

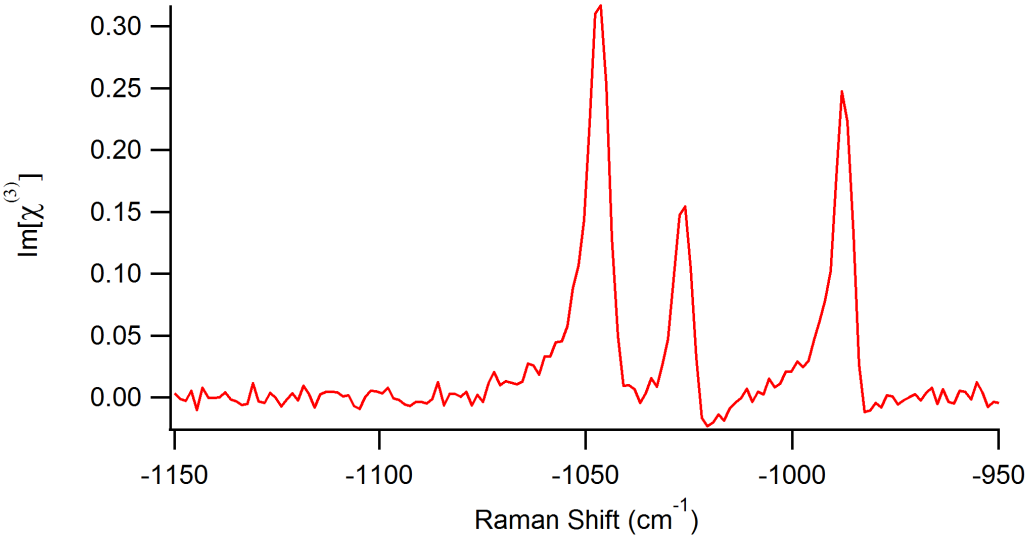

Figure s3. CARS spectrum of 500 mM of pyridine **1** in dichloromethane-d_2

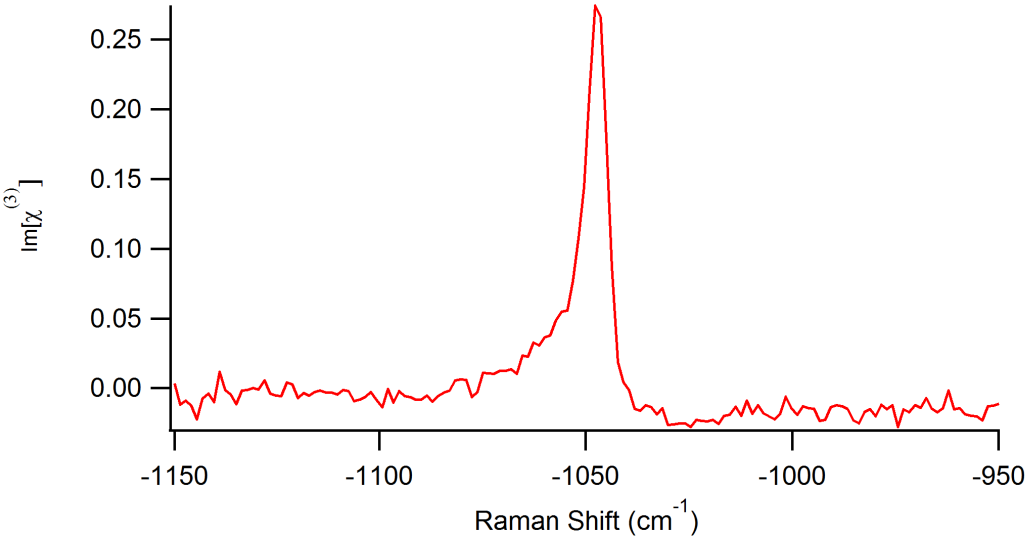

Figure s4. CARS spectrum of 500 mM of hexafluoroisopropanol **2** in dichloromethane-d_2 within the model measurement window (only the signal of the solvent is present).

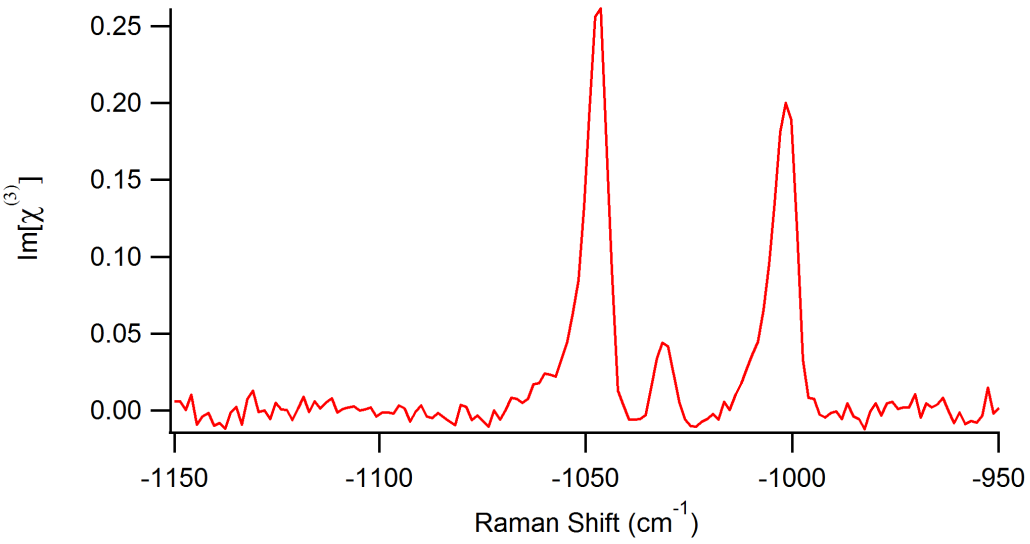

Figure s5. CARS spectrum of complex **3** (pyridine×hexafluoroisopropanol**)** in dichloromethane-d_2 (concentration of components in the solution: 500 mM of pyridine **1** and 750 mM of hexafluoroisopropanol **2**; the concentration of uncomplexed pyridine **1** is 6,4 mM [1,3% in comparison with 493,6 mM of complex 3] and its signal is below the noise level).

3. Data Analysis

The analysis of CARS spectra is complicated by the convolution of the vibrationally resonant term, with a nonresonant term arising from the electronic response of the material. Spectra of the imaginary part of the third-order nonlinear susceptibility, Im[$\chi^{(3)}$], were retrieved from the raw CARS spectra by the maximum entropy method (MEM). It is important to point out that all the treatments of raw experimental and calibration spectra should follow the same algorithm, mem-parameters, mask for the baseline removal, areas for the integration of signals, etc.

a. MEM treatment of raw CARS data

Upon the acquisition of CARS spectra, CARS.NET and DeLorean.NET save data in the .FITS format. This data can be read into Igor Pro, passed through the Maximum Entropy Method (MEM) algorithm and subjected to further processing using the following suite of procedures. The standard MEM treatment of the raw CARS data in Igor Pro (using mem_launch.pxp program):

1. Run the dividebyref() procedure. This procedure normalizes the CARS data according to the equation: CARS = (CARS−bckgspec)/(refspec−bckgspec)
2. Run the memprep(rsmin,rsmax) procedure. This procedure will truncate the frequency range of the data over which the MEM procedure will run. *rsmin* and *rsmax* are the minimum and maximum frequencies of the truncation window, respectively. The outputs are:
   - m_ramanshift
   - m_cars
   - m_spectrum
3. Run the memit(autocorr) procedure. This is the main program that performs the MEM algorithm using *autocorr* as the number of autocorrelations. It outputs the phase and Im[$\chi^{(3)}$] spectra as:
   - phase_data
   - imchi3_data
4. To perform an error phase correction, use a low-order polynomial together with a mask. The mask has to be created manually – typically we would use the following commands:
   - Duplicate /o phase mask
   - Mask=1
   - ShowInfo //place cursors around peaks in the phase spectrum
   - Mask[pcsr(b),pcsr(a)]=0
   - Curvefit /q poly n, phase /m = mask /d

   These commands give a test fit of the error phase. To perform the error phase correction on the entire data set with the same mask, run the epsubtr(n) command, where *n* is the polynomial order.
5. The final output is the imchi3_data_b wave.

The standardly used mem parameters: rsmin = -1150, rsmax = -950, autocorr = 500, n=6.

b. Further steps in the initial analysis

1. If the CARS experiment consists of several consecutive measured areas, these separate imchi3_data_b waves are combined.

2. Defect spectra (around 1-2 of 1000) are manually replaced by the average of the neighboring spectra.

3. Integration of the peaks. The preferential approach is the automatic calculation of integral intensities of nonoverlapping areas of the signals of interest (examples of the integrated areas cm^{-1}: solvent, dichlorometane-d_2, signal: 1070 to -1045; complex **3** signal: -1010 to -1000; pyridine 1 signal: -999 to -980). Alternative approach of fitting of the signals to Lorentzian or Gaussian curves was also performed, however it is less preferential for the automatic analysis of the thousands of CARS spectra due to the asymmetry and the presence of the negative components of some signals in a number of spectra.

This analysis results in the microscopic image of the reaction progress with respect to the change in the signals intensity. The changes in the intensity of the signals of the solvent

(dichlorometane-d_2), pyridine **1**, and complex **3** are shown in Figures s6a, s6b, and s6c respectively.

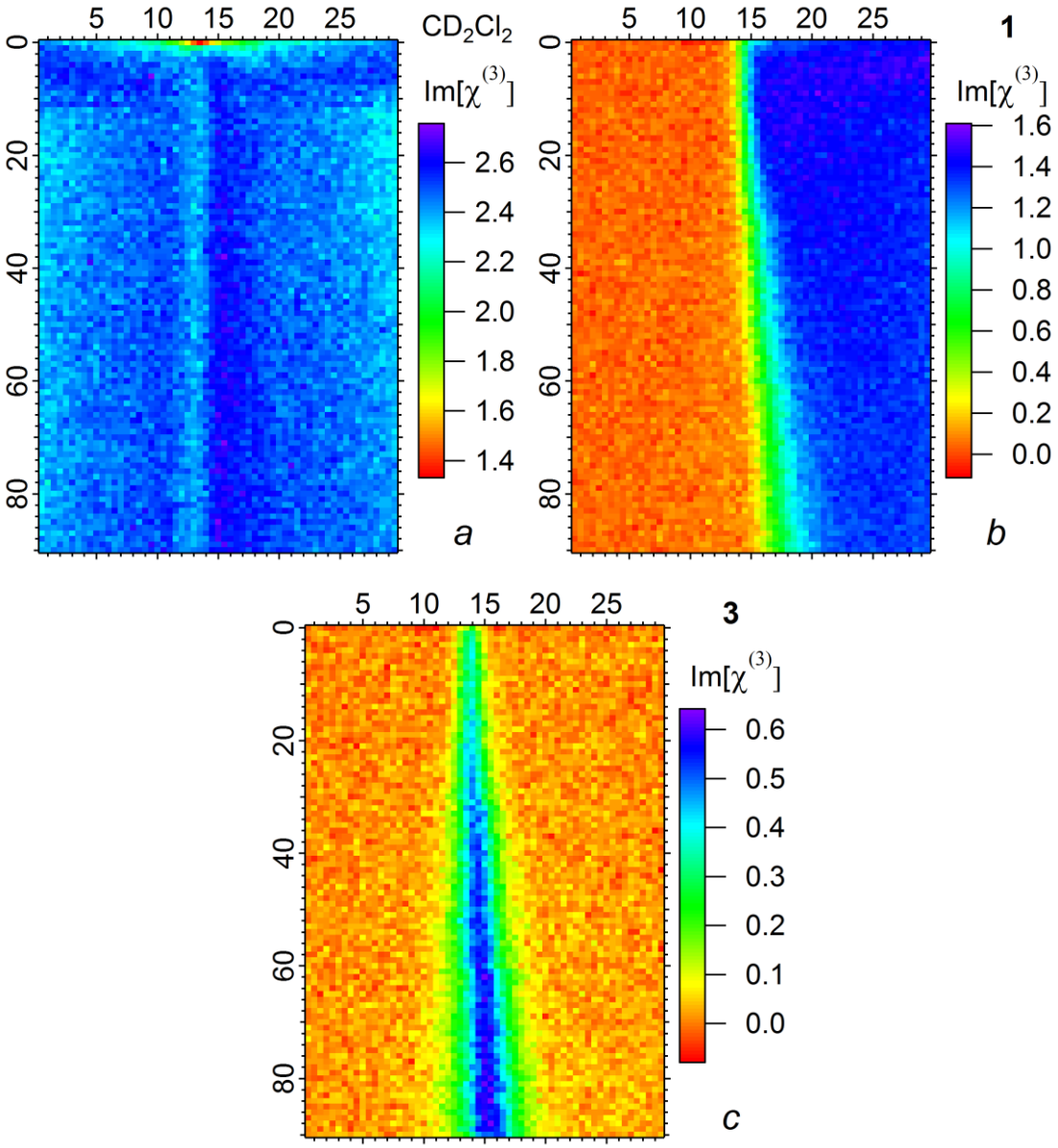

Figure s6. Absolute signal Intensity of the solvent and reacting species.

4. Determination of the ratios of the signal to the solvent reference. This is achieved by division of the waves of absolute signal intensity of pyridine and complex **3** by that solvent. The resulting waves presenting the change of I_{Py}/I_{CD2Cl2} and $I_{PyxHFiP}/I_{CD2Cl2}$ across the channel are shown in Figure s7a and s7b, respectively.

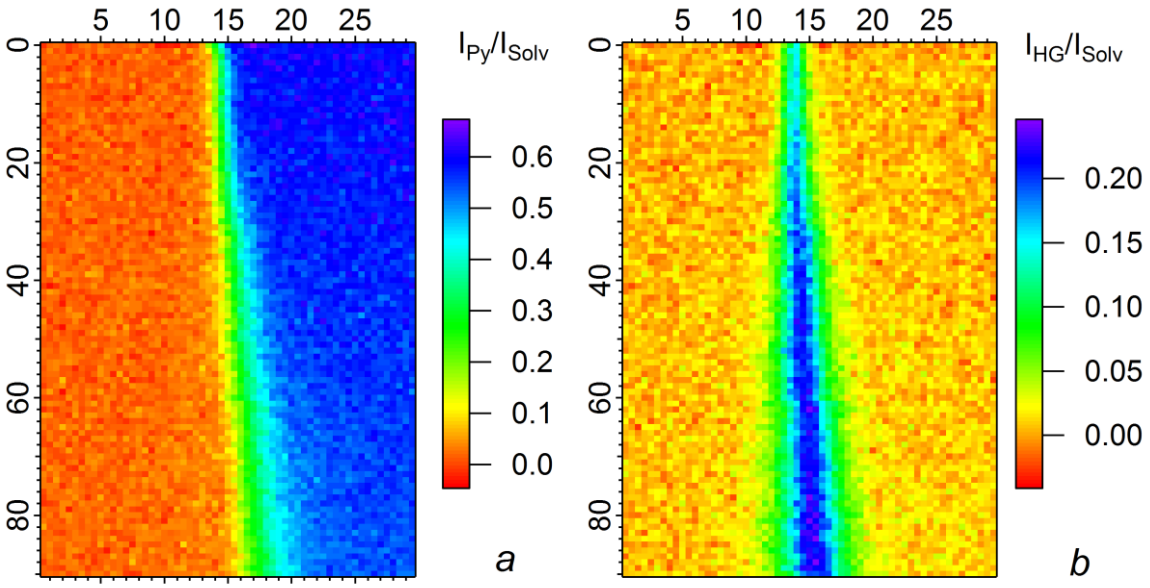

Figure s7. Ratio of signal Intensities

c. Calibration

To obtain the concentration values from the intensity and the ratio of intensities values, a calibration curve method was used. Four solutions containing different concentrations of the interacting components were measured 100 times (areas 10x10 spectra). The chemical composition of the equilibrium mixture (Scheme s1) present in these solutions, based on K_a = 300 M^{-1} for this interaction, is shown in Table s1. Average values of the signal intensities and the ratio of the signal intensities to the reference were plotted to the known concentrations of components of the supramolecular equilibrium.

Table s1. Equilibrium concentrations of the model equilibrium.

	Concentrations, M				
	Pyridine (total)	HFiP (total)	[1]	[2]	[3]
0	0.500	0.000	0.500	0.000	0.000
1	0.500	0.100	0.401	0.001	0.099
2	0.500	0.250	0.253	0.003	0.247
3	0.500	0.500	0.039	0.039	0.461

Examples of the calibration data: Intensity of the host-guest complex signal:

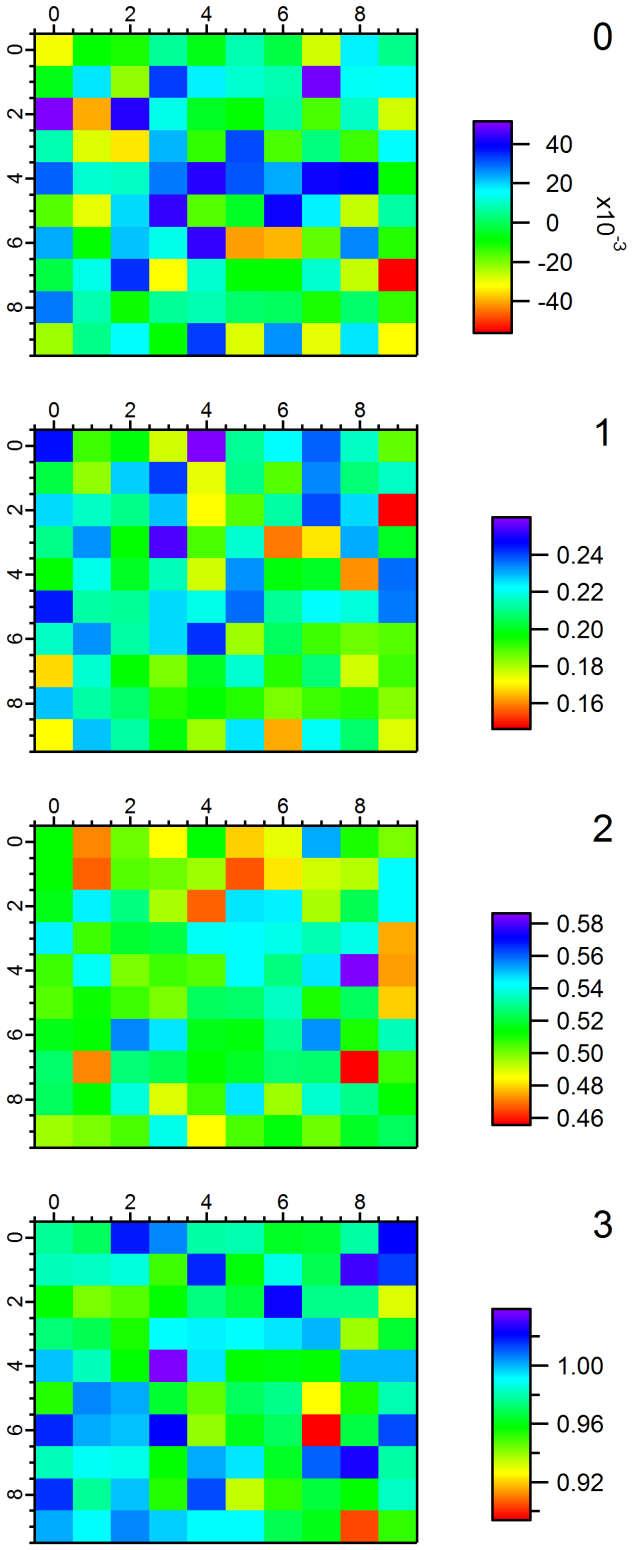

Figure s8: Calibration Points of HG complex **3**

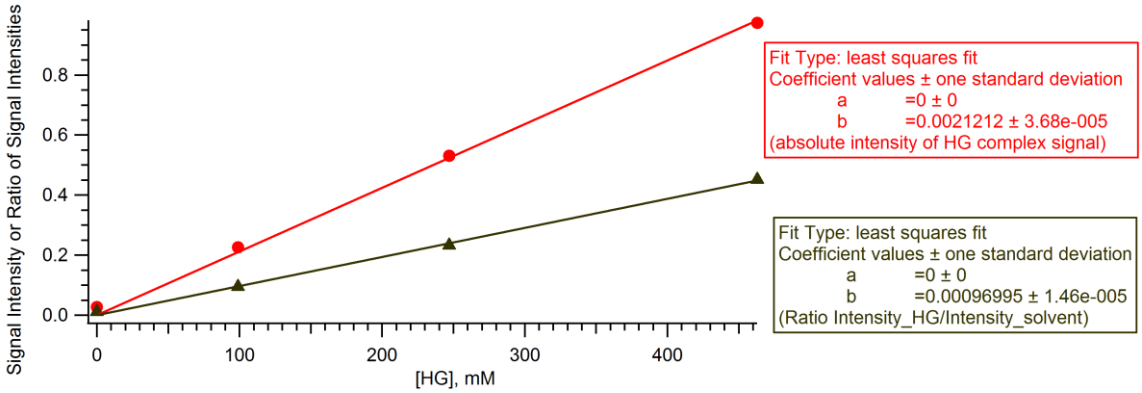

Figure s9: Examples of fitted calibration data of HG complex **3**

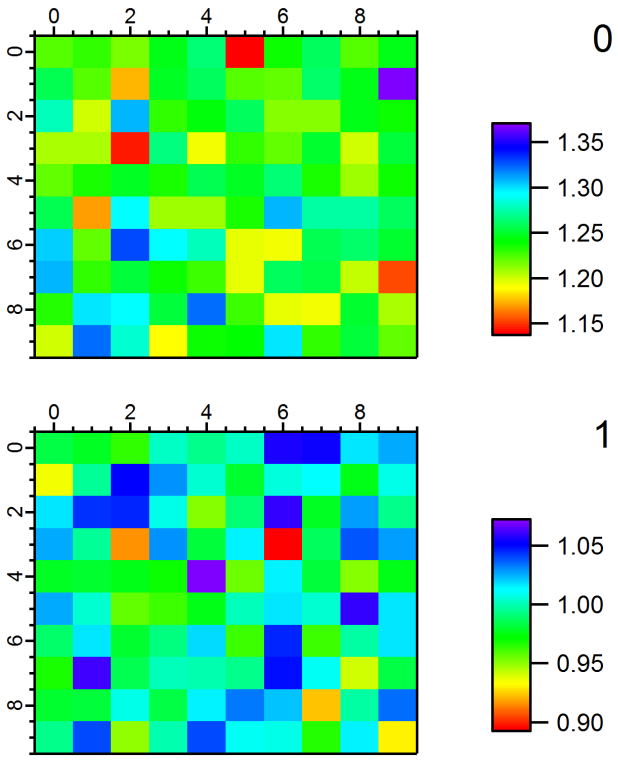

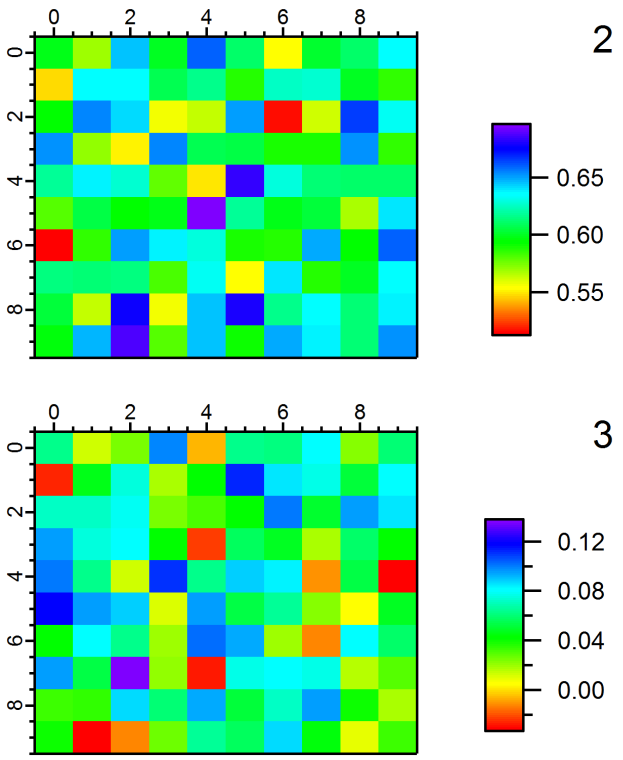

Figure s10: Calibration Points areas of pyridine **1**

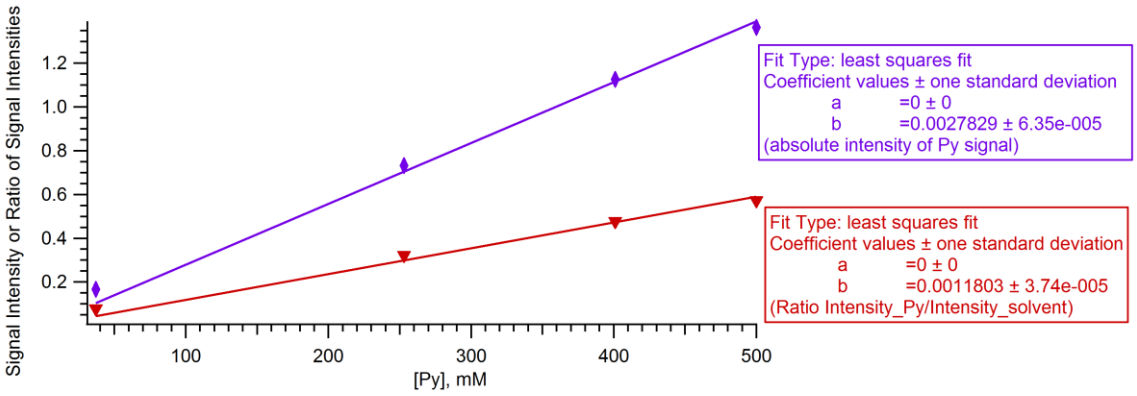

Figure s11: Examples of fitted calibration data of pyridine **1**

The coefficients ***b*** obtained with the fitting (to a line y = bx) are used in the direct and ratio methods (see section 3e of this supporting information).

d. Direct and Ratio Methods

Direct and ratio methods are approaches used to obtain the concentrations from the intensities in the CARS experiments based on the calibration data.

I. Direct method

It uses the absolute intensity of the measured signals. To apply this method, the normalization of intensities is necessary, which consists in the use of a normalization coefficient (k_{norm}):

$$k_{norm} = I^*_{calibr} / I^*_{exp}$$

It presents a ratio between average intensities of CARS signals of an analyte *at the same concentration* in a calibration (I^*_{calibr}) and in a real experiment (I^*_{exp}), to account for possible experimental differences between the calibration and experimental sets. In this paper, I^*_{calibr} is the average intensity of the pyridine signal in the calibration experiment **0** ([Py] = 500 mM, see Table s1), as shown in Figure s 12a. I^*_{exp} is an average intensity in the area of microchannel on the side, where 500 mM solution of pyridine in CD_2Cl_2 is injected in the area, where no formation of complex **3** takes place (Figure s 12b). I^*_{calibr} and I^*_{exp} are not the same due to the collection of the calibration spectra in non-problematic areas of the chip, not in the vicinity of junctions; even more, different CARS laser power can also be applied in the calibration and real experiments.

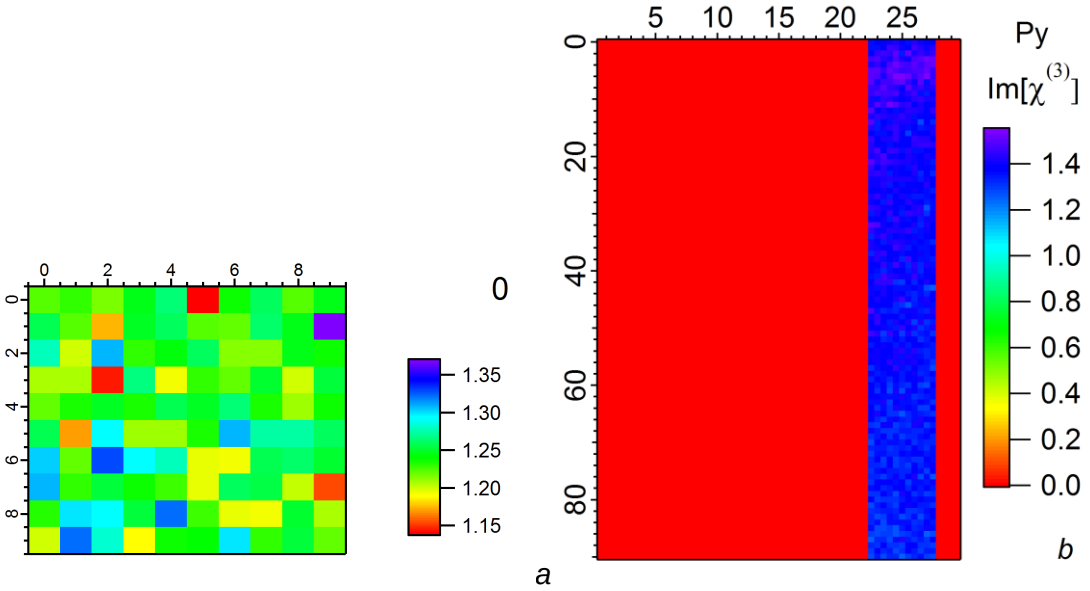

Figure s 12. I^*_{calibr} (a) and I^*_{exp} (b)

The concentration in every measured area (Conc) is determined with the equation:

$$Conc = I \times k_{norm} / b$$

(I - intensity of the CARS signal (of its non-overlapping part); k_{norm} - normalization coefficient; b - coefficient of the absolute intensity calibration curve: y = bx)

Disadvantages of the direct method: it is very sensitive to the chip effects, laser power variations, and signal intensity drift (which complicates the determination of the exact value of I^*_{exp}. as shown in Figure s14)

II. Ratio method

This method uses the ratio between the absolute intensity of a signal of ineterest (I) and that of a signal of the reference compound (I_{ref}): I/I_{ref}. In this paper, the signal of the solvent, dichloromethane-d_2 is the reference signal. In the ratio method no normalization is necessary. Hence, this approach is resistant to the chip effects and the variations in the CARS laser power.

In the ratio method, the concentration in every measured area (Conc) is determined using the following equation:

$$Conc = (I/I_{ref}) / b$$

(I/I_{ref} - ratio of CARS signal intensities; b - coefficient of the ratio intensity calibration curve: y = bx)

Disadvantages of the ratio method: since the solvent signal was used as a reference, slight variations in the molar fraction of the solvent (see, for example, Figure s6a) will influence the output of the method. This effect is pronounced only in very concentrated solutions. The possible alternative in the future is an added reference compound, provided its inertness to the studied process and good solubility in the reaction medium.

III. Chip effect and Signal intensity drift

Microchannels have defects (different thickness and optical properties of a material above the channel, as clear from the figure s13) that is the most pronounced in the vicinity of junctions. This influences the absolute intensity of the CARS signals, but not the ratio of the signals. Therefore, the ratio method helps to account for the chip effects.

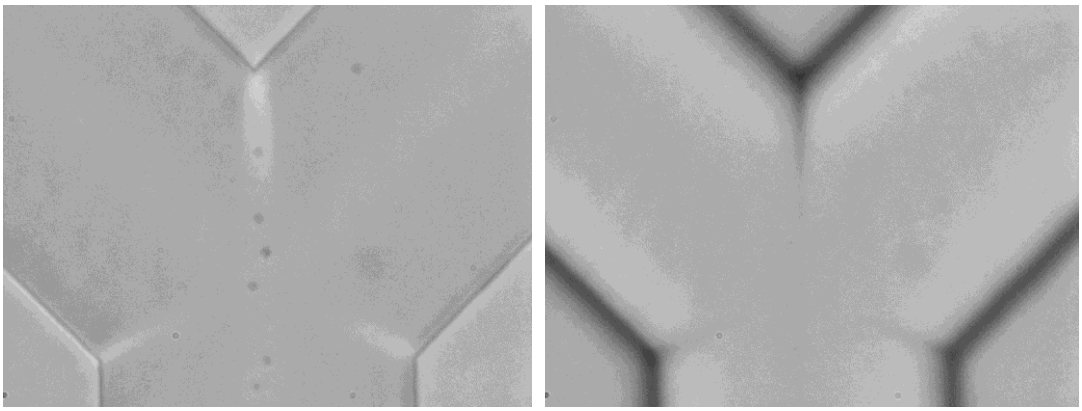

Figure s13. Optical images of the microchannels; *defects, especially that in the vicinity of junction are clearly visible.*

The signal intensity of some measured compounds (slightly) changes across the channels, even in the areas where the chemical composition stays the same (Figure s14). This phenomenon is named here a signal intensity drift.

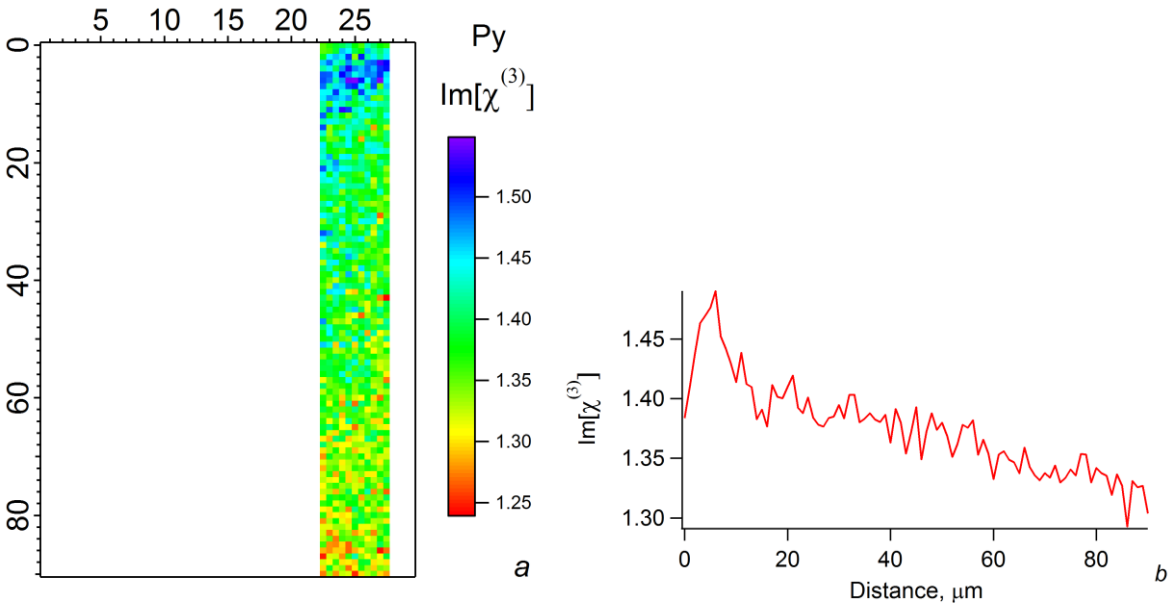

Figure s14. Signal Intensity drift

e. Application of the calibration data

The application of direct or ratio methods leads to revealing the reagents concentration changes across the microchannel (see, for example Figure s15 for 2D and Figure s16 for 3D presentations).

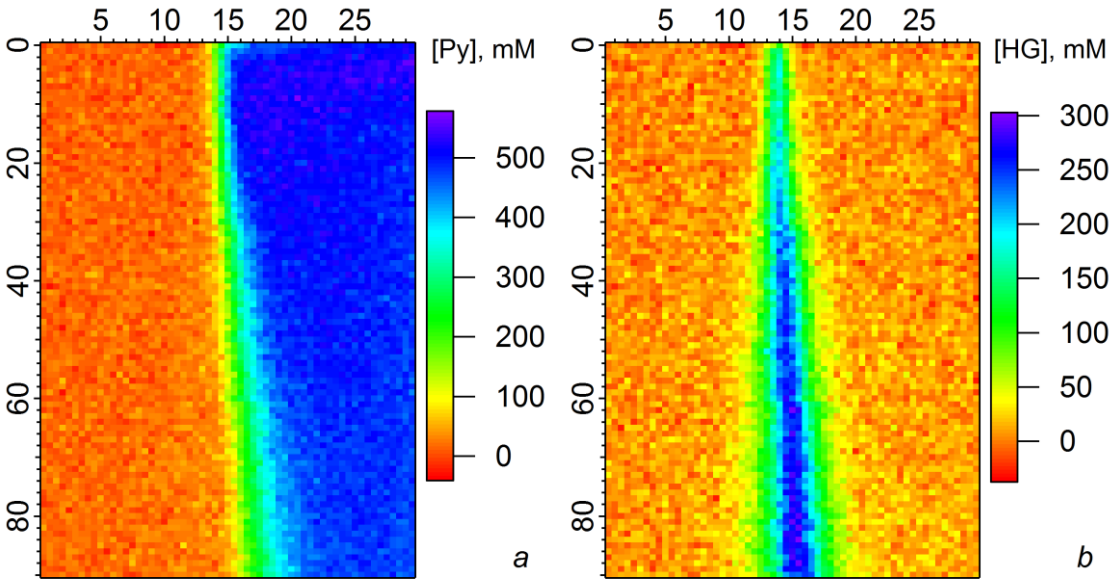

Figure s15. Progress of the reaction in terms of concentrations

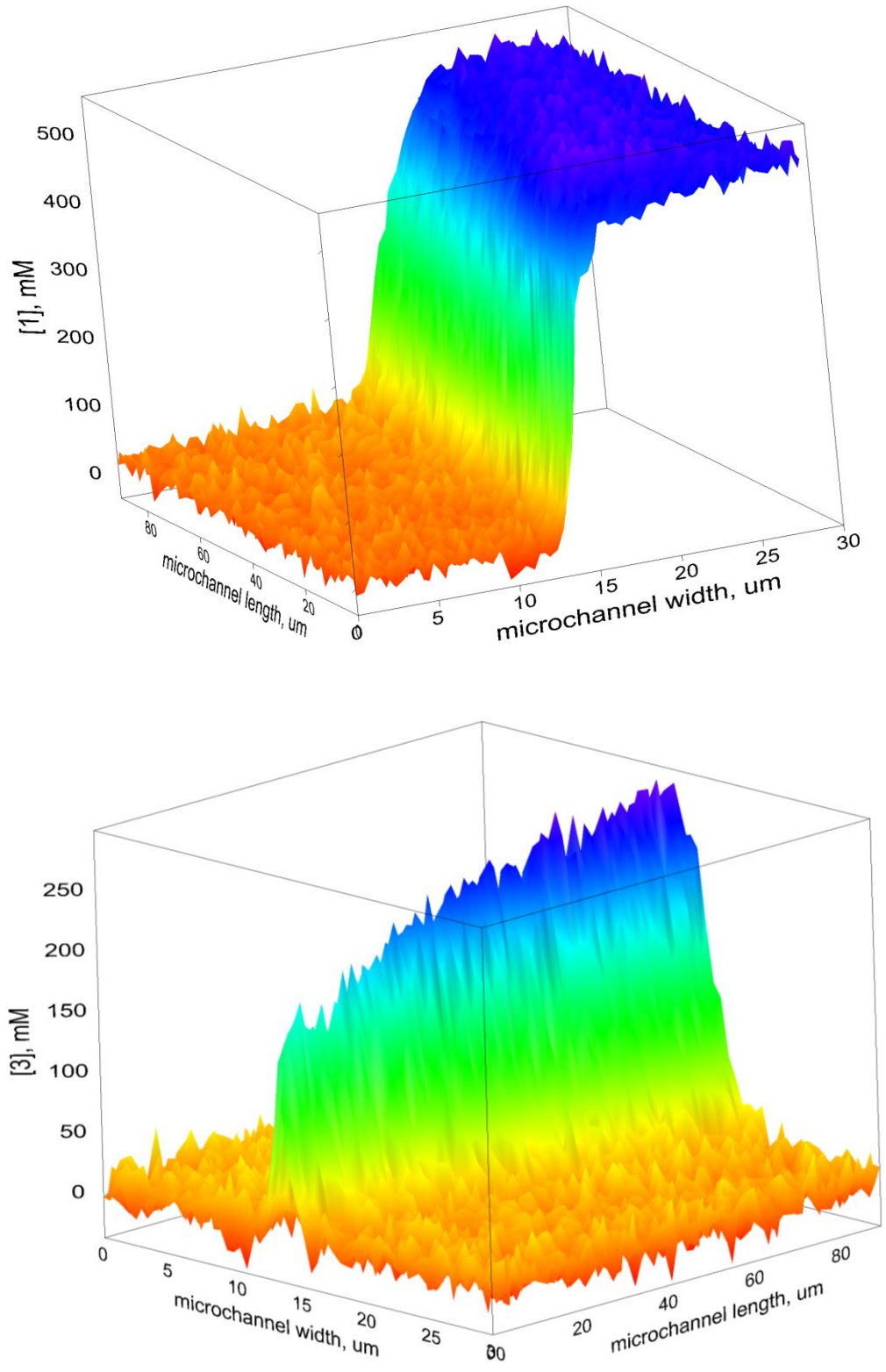

Figure s16. 3D-Images presenting the progress of the reaction in terms of concentrations

f. Fit of the experimental calibrated data

The fitting of the spectral areas at every micrometer in the direction of the flow (examples of the fit are shown in Figures s17) leads to the minimization of the background noise influence. In the course of fitting, the background is fixed to zero.

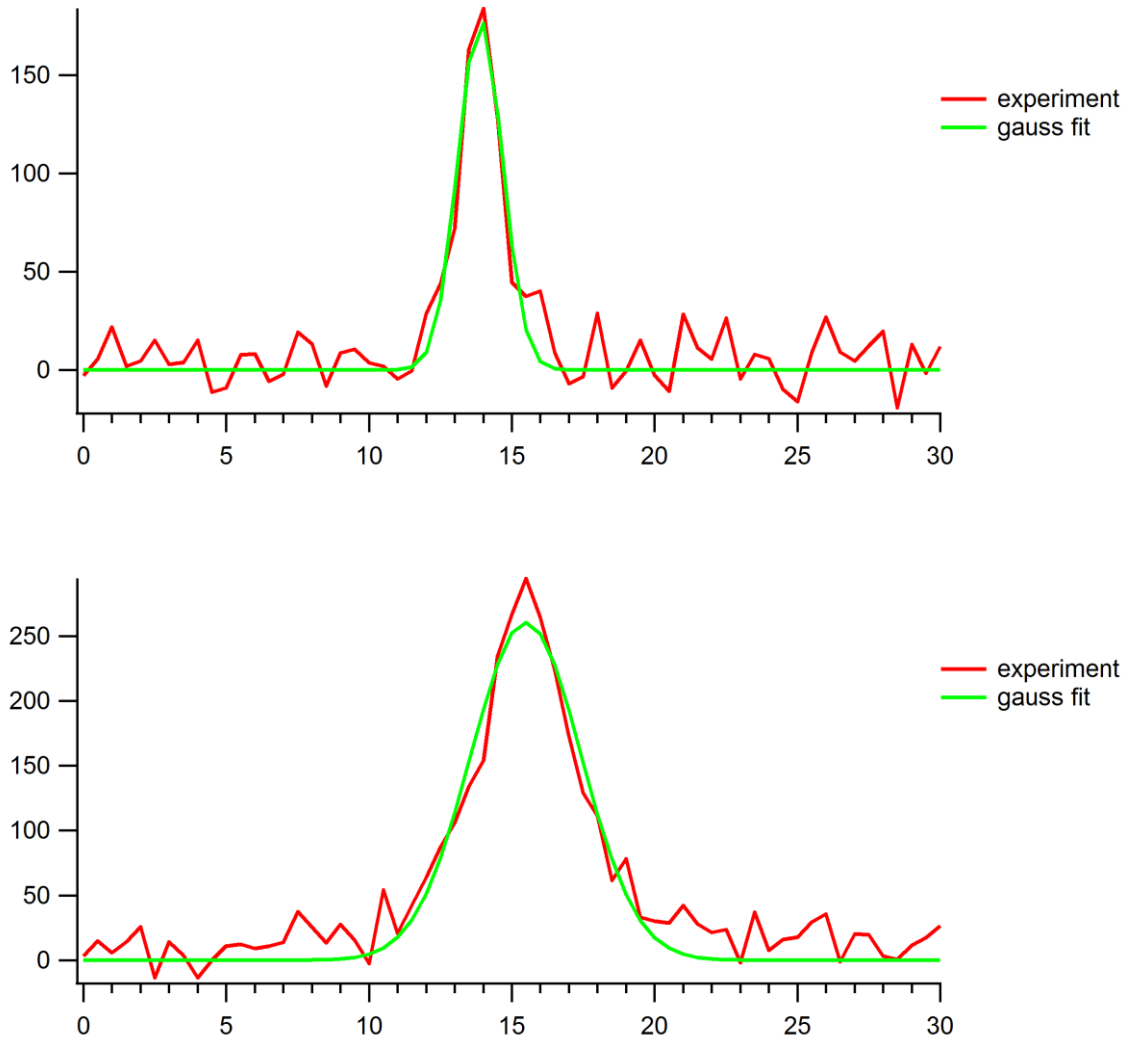

Figure s17. Examples of a Gaussian fit to the experimental data perpendicularly to the flow at the different places across the channel.

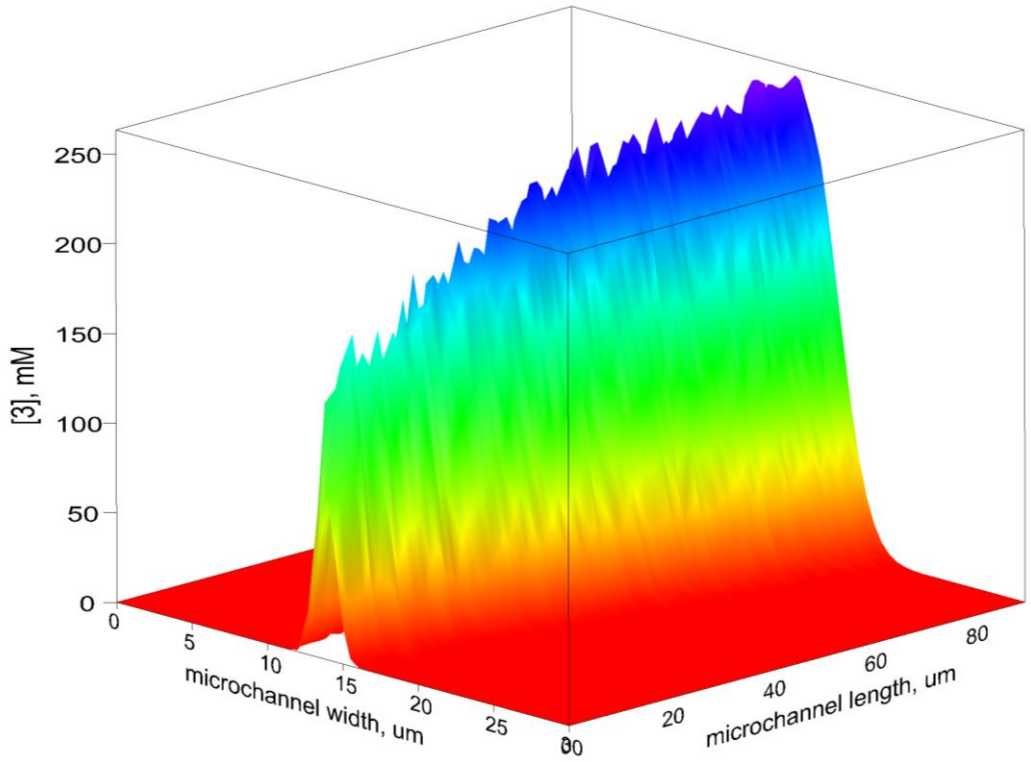

Figure s18. The progress of the reaction in the microchannel: 3D-Images of the fitted calibrated signal Intensity

g. Integration

Integration of every of Gaussian curves leads to the 2D experimental curves presenting the increase of integral concentration of complex 3 versus distance in the microchannel in the direction of the flow. Examples of such curves are shown in Figure s19. The direct method gives slightly higher values of integral concentrations in comparison with the ratio method.

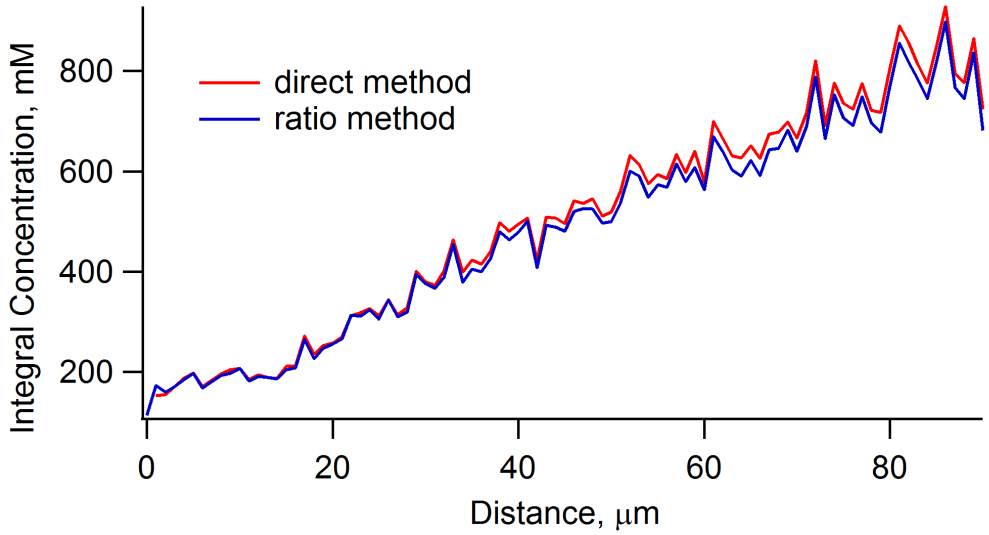

Figure s19. Progress of the complex **3** formation across the microchannels.

4. Modeling with COMSOL Multiphysics (v 4.2)

The 2d-modelling was performed in an area resembling an Y junction, with a condition of a non-turbulent mixing of two solutions. The modeling results in the flowrate profile and the progress of the reaction across the microchannel. The input parameters are diffusion coefficients of pyridine **1**, hexafluoroisopropanol **2**, and complex **3** (pyridine×hexafluoroisopropanol) in dichloromethane-d2, as well as the diffusion coefficient of the solvent itself. These are determined using DOSY NMR (see section 5b of this supporting information).

a. Flowrate modeling

The change of the flowrate of liquids across the microchannel upon mixing of two solution (Figure) is responsible for the extra bending of the kinetic curve.

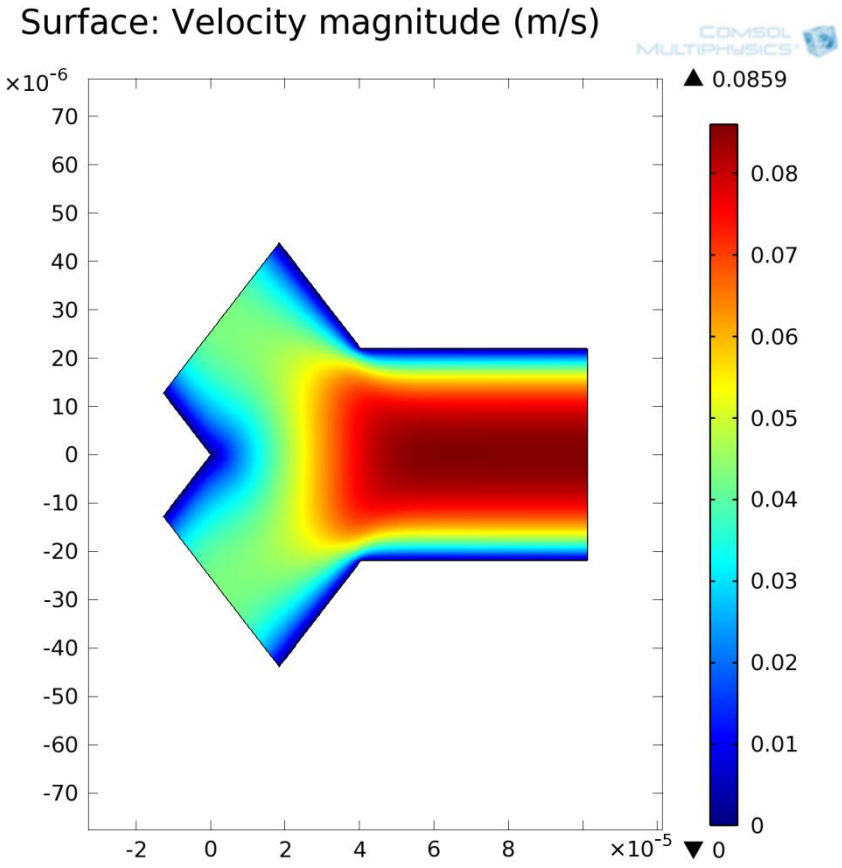

Figure s20. The solutions flowrate profile in the microchannel around the Y-junction.

b. Reaction progress

The modeling was performed for the variation of k_1 from 10 $m^{-1}s^{-1}$ to 10^7 $m^{-1}s^{-1}$. Images presented in a figure below present the results of this modelling.

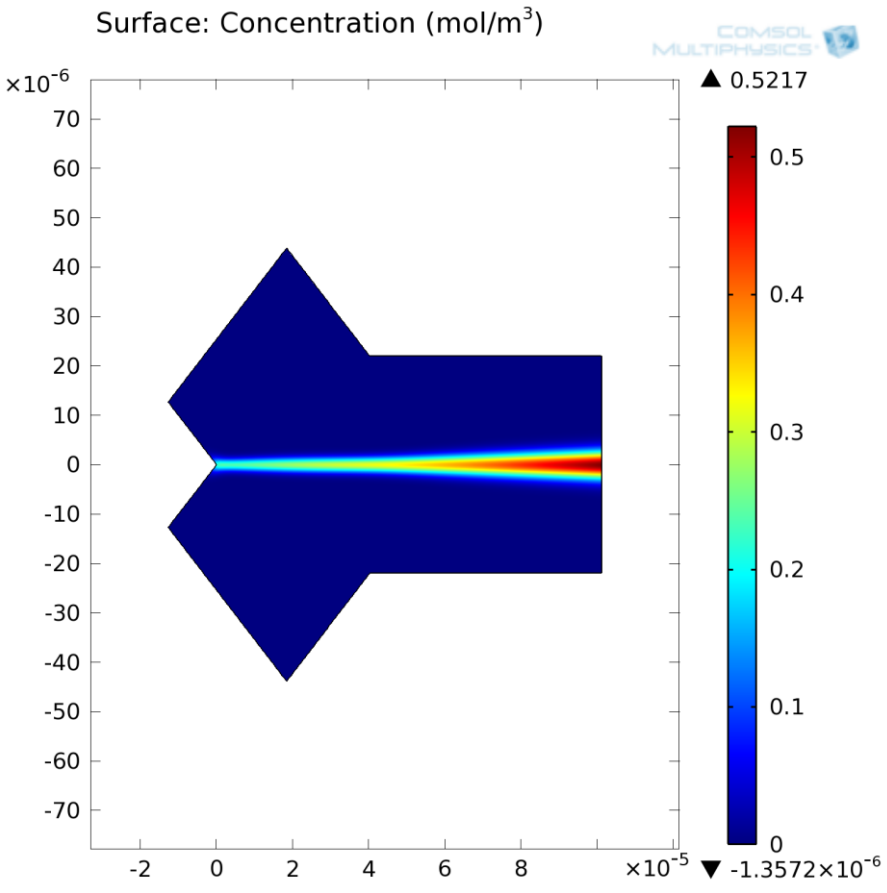

10 $m^{-1}s^{-1}$

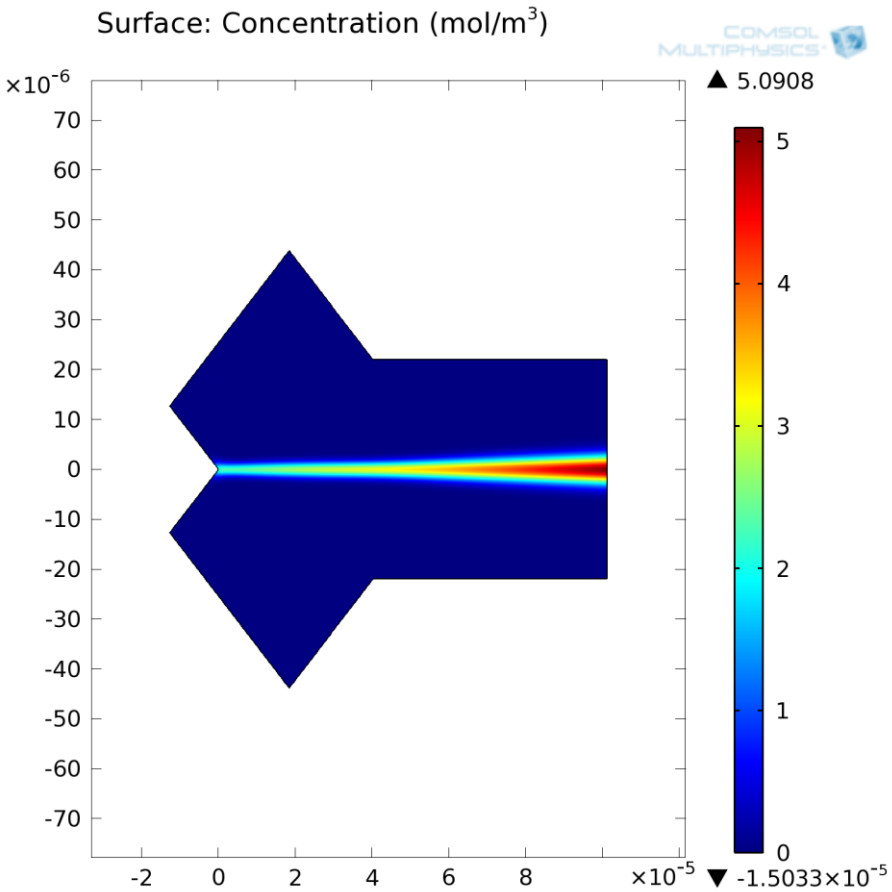

100 $m^{-1}s^{-1}$

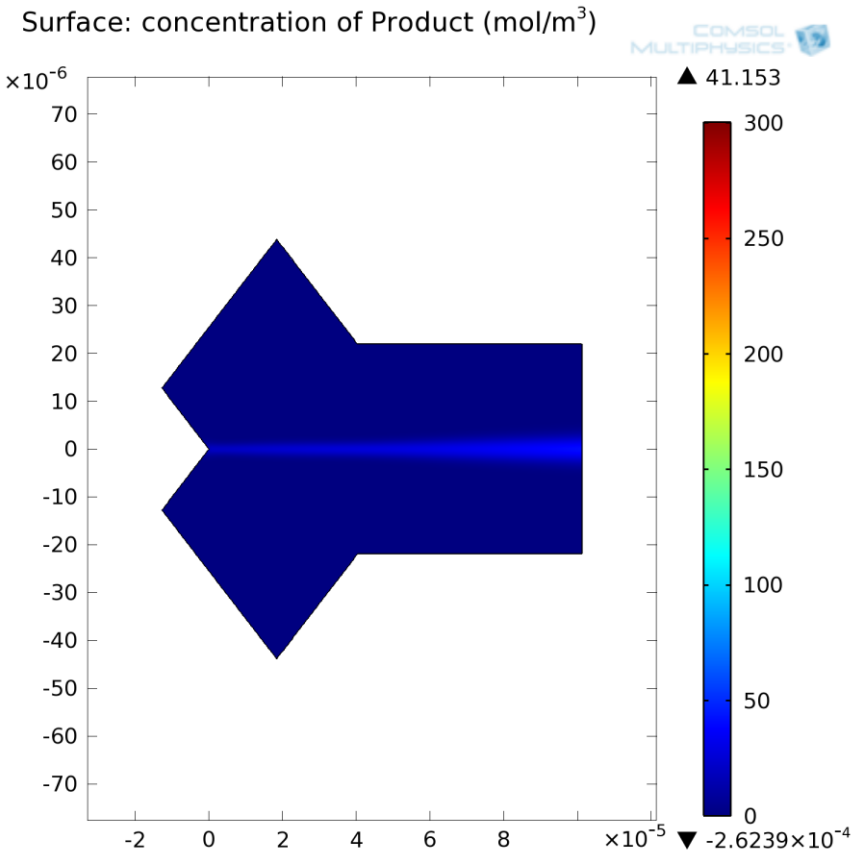

1000 $m^{-1}s^{-1}$

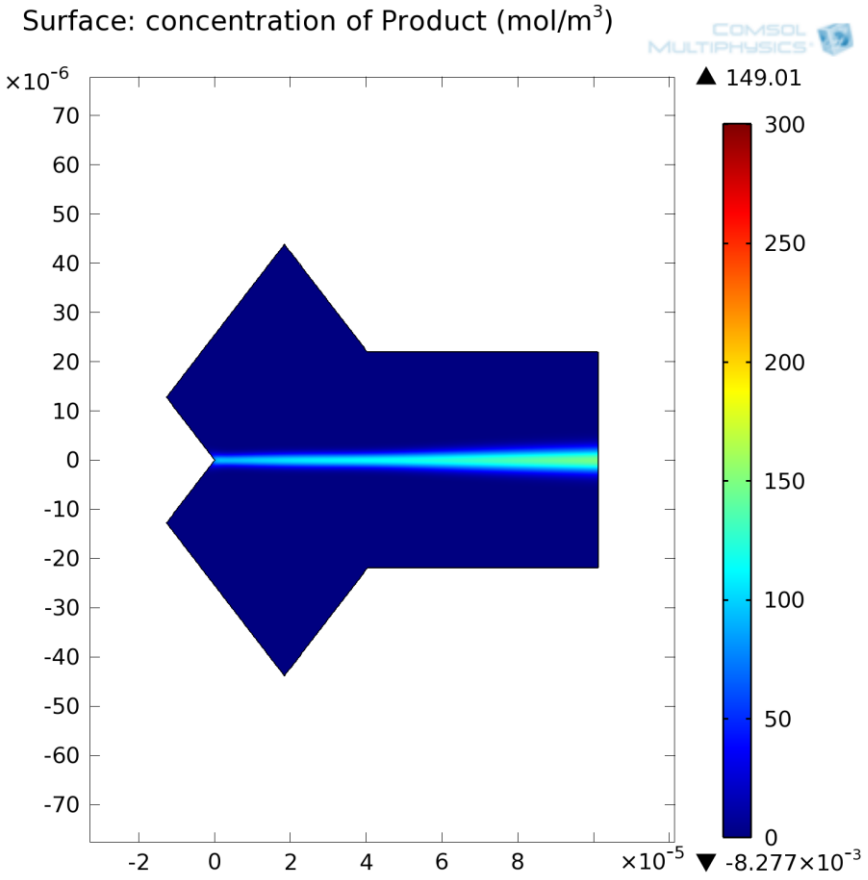

10000 $m^{-1}s^{-1}$

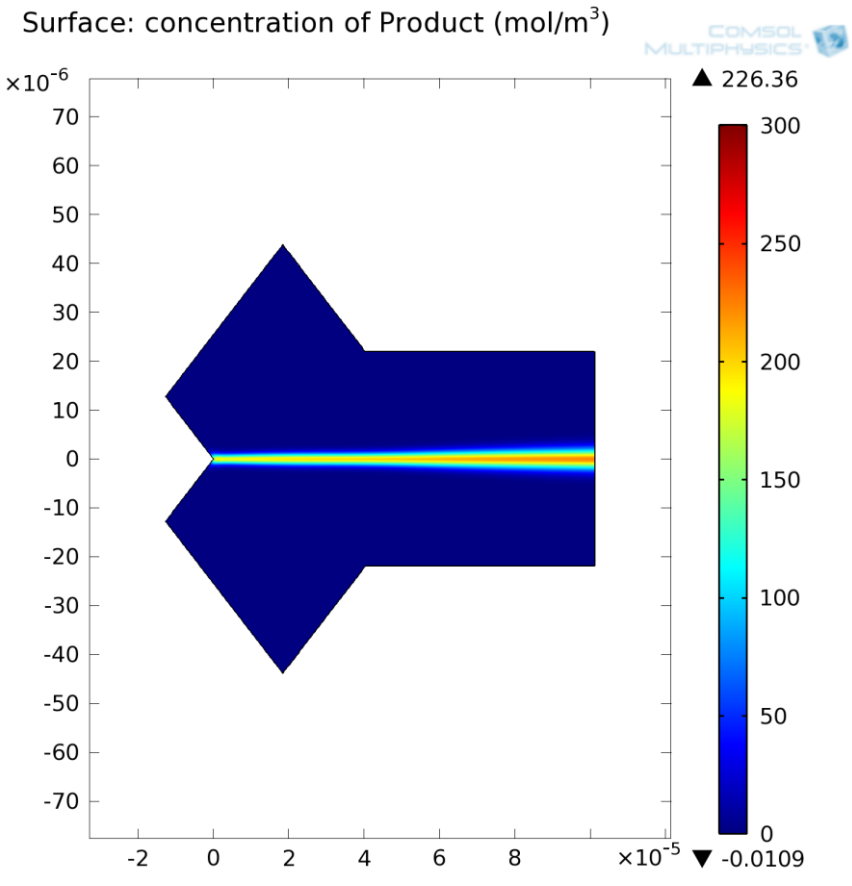

10^5 $m^{-1}s^{-1}$

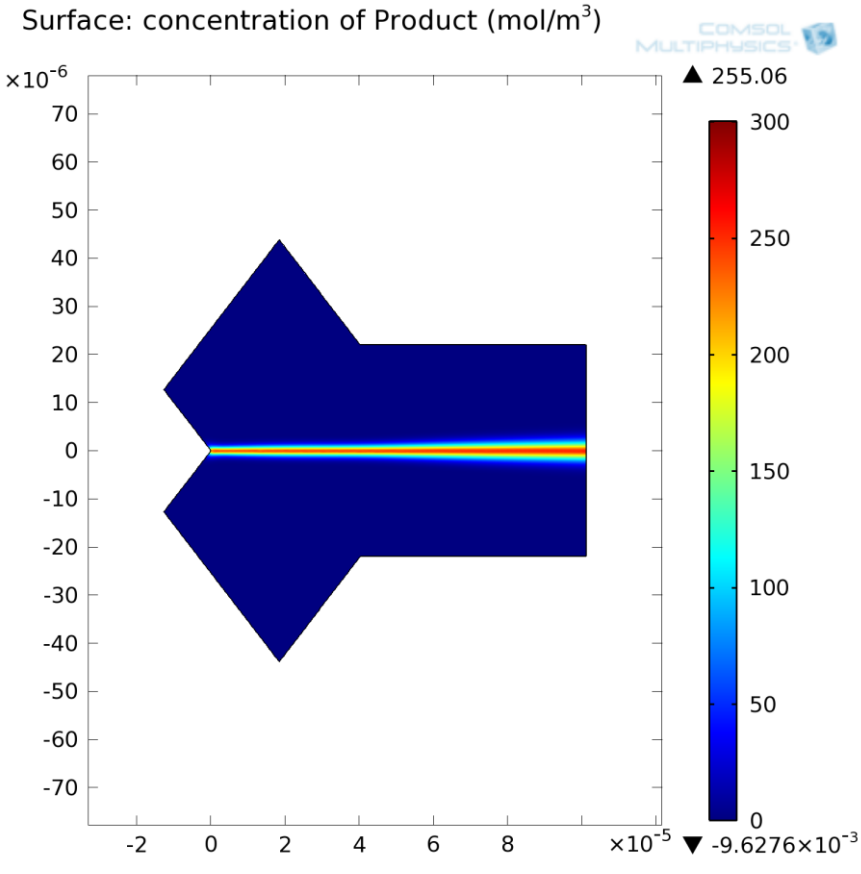

10^6 $m^{-1}s^{-1}$

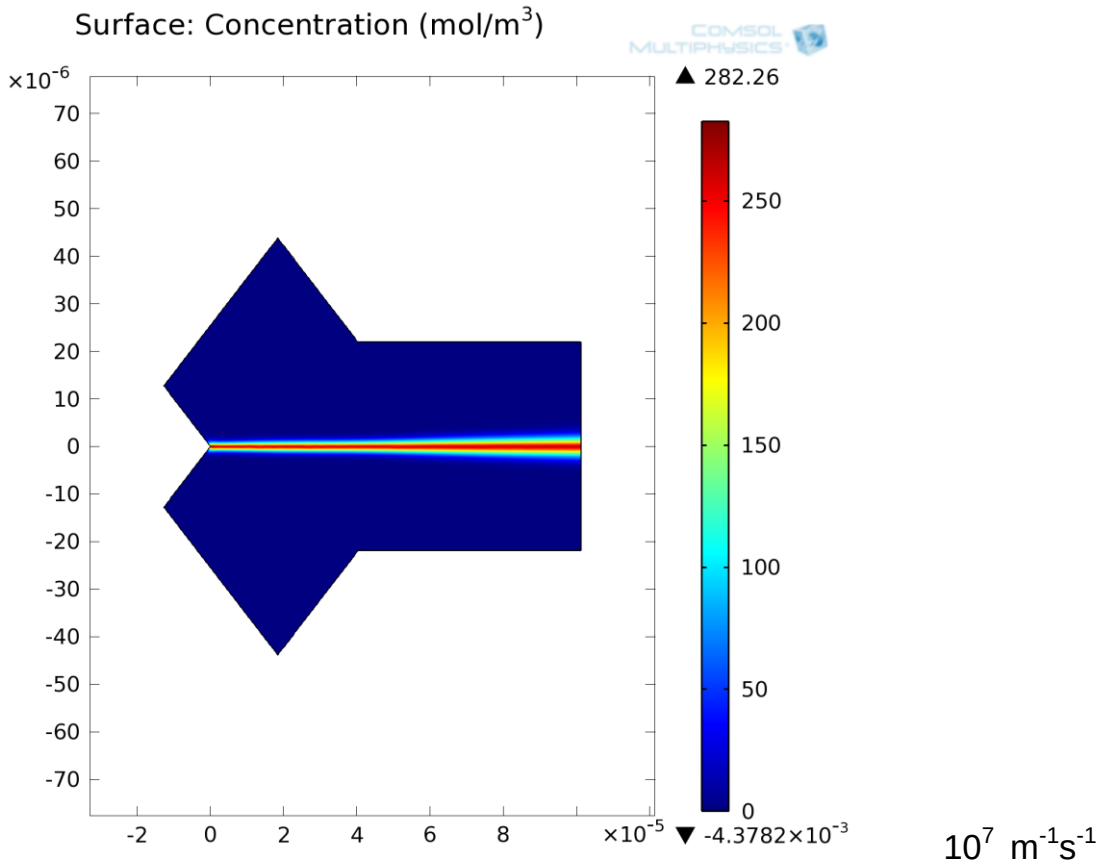

Figure s21. The modeled progress of the formation of complex 3 depending on k_1

c. Data transfer to Igor Pro and Integration

A rectangular grid of data of the dimensions (x: from 0 to 90 μm, step 1 μm; y: from -15.25 to +15.25 μm, step 1nm; zero point is the beginning of the junction where two flows first meet each other) is saved from COMSOL multiphysics as a *.txt file. The data are loaded to Igor Pro (examples of 2D and 3D images of the kinetic data for k_1 = 10^6 $m^{-1}s^{-1}$ are shown in Figure s22). The fitting the data at every micrometer in the direction of flow followed by the integration of the curve areas gives a 2D presentation of the reaction progress in terms concentration of complex **3** *vs* distance (example of the curve for k_1 = 10^6 $m^{-1}s^{-1}$ is shown in Figure s23, collected image is presented in Figure s24).

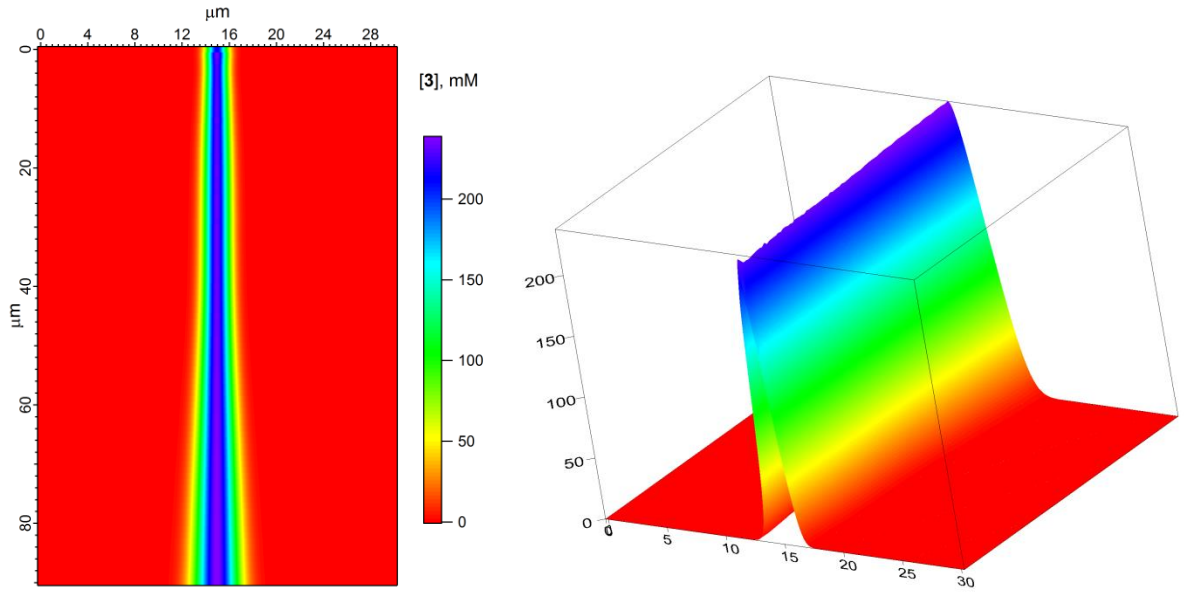

Figure s22. Examples of the COMSOL multiphysics data transferred to IgorPro; the resolution of the modeling in the direction of the flow is 1 µm, and that perpendicular to the flow is 1 nM.

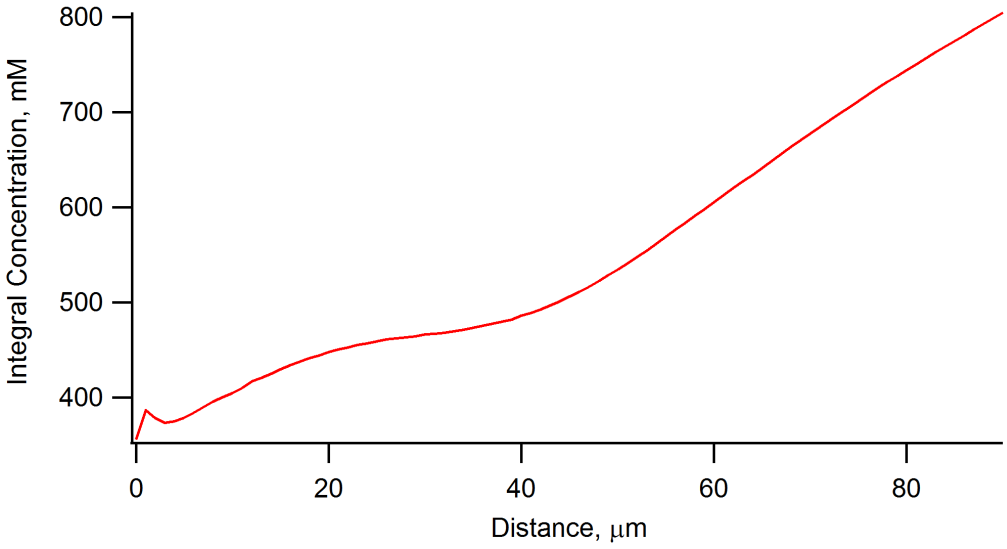

Figure s23. Image of the reaction progress for $k_1 = 10^6$ $m^{-1}s^{-1}$.

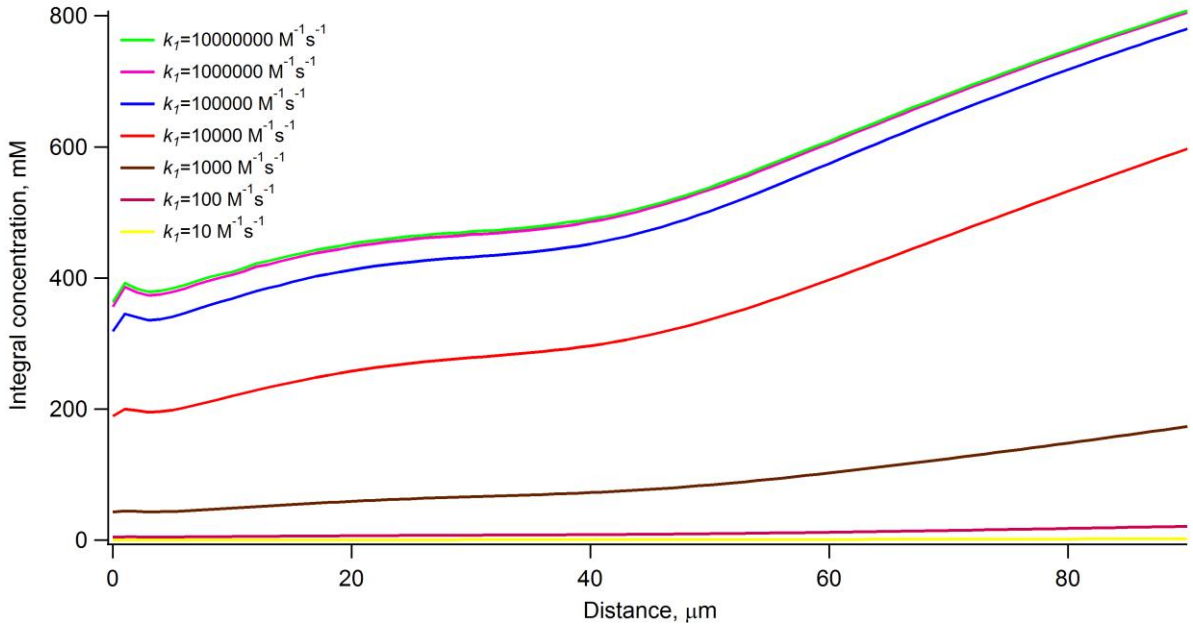

Figure s24. Collected image of the reaction progress.

5. NMR Studies

NMR Varian Mercury-VX (300 MHz) was used for the measurements of ^{19}F NMR spectra. Diffusion PGSE (Pulsed-field Gradient Spin Echo) NMR experiments were performed on Bruker DRX300 (300 MHz) apparatus.

a. Stability Constant

The stability constant was determined by ^{19}F NMR titration in dichloromethane-d_2 by the addition of the solution containing pyridine and hexafluoroisopropanol to the solution of hexafluoroisopropanol, so that the concentration of hexafluoroisopropanol stays constant. The titration was performed twice with 16 titration points. Fitting (1:1 binding model, Excel based application using solver, Figure s25) provides K_a = 300 M^{-1} (± 6). Twelve (12) of the 16 titration points are located within 20-80% of the maximal complex formation (validation of the data quality with the Weber rule[2]).

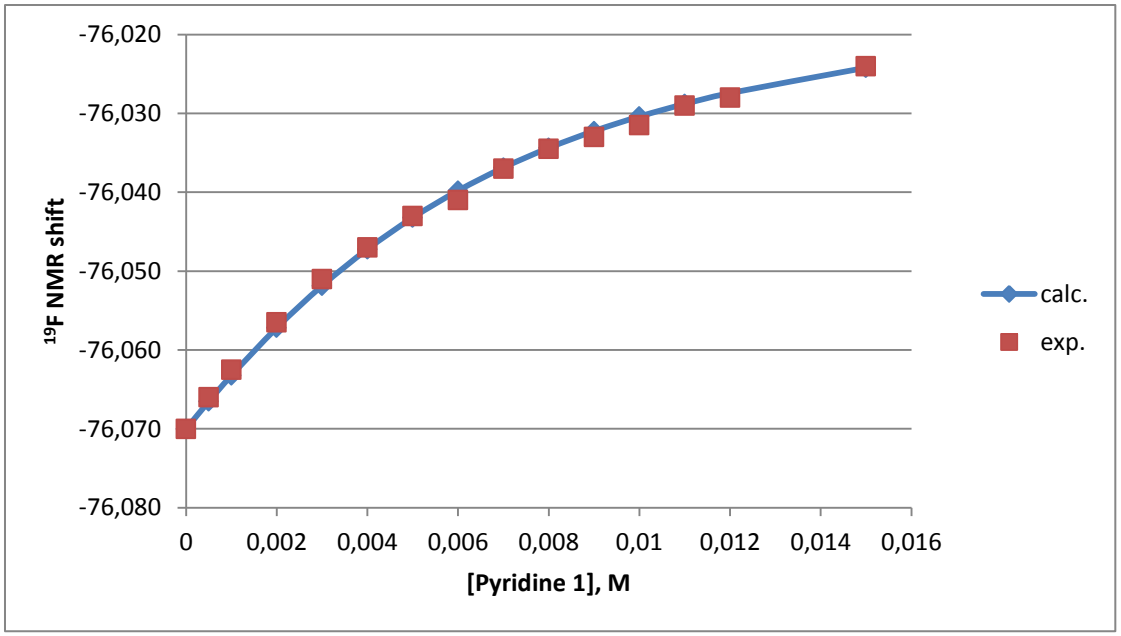

*Figure s25: ^{19}F NMR titration data of hexafluoroisopropanol **2** by pyridine **1*** (experimental points and fitted curve).

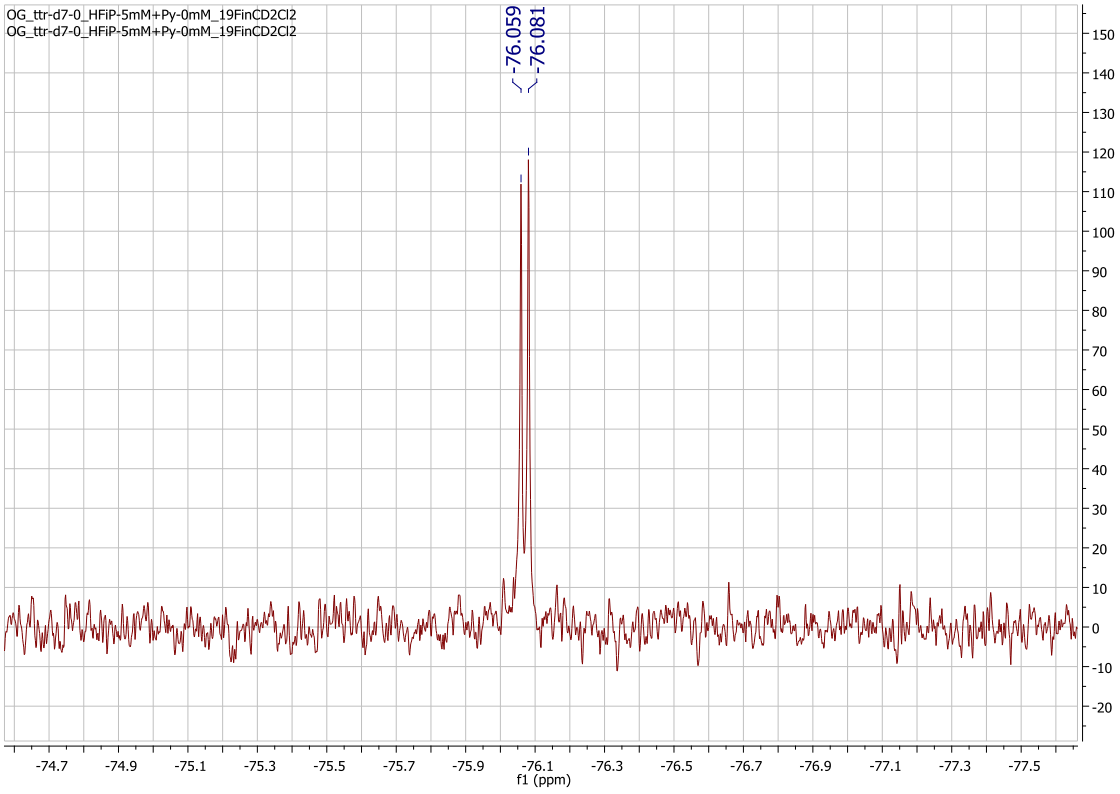

a

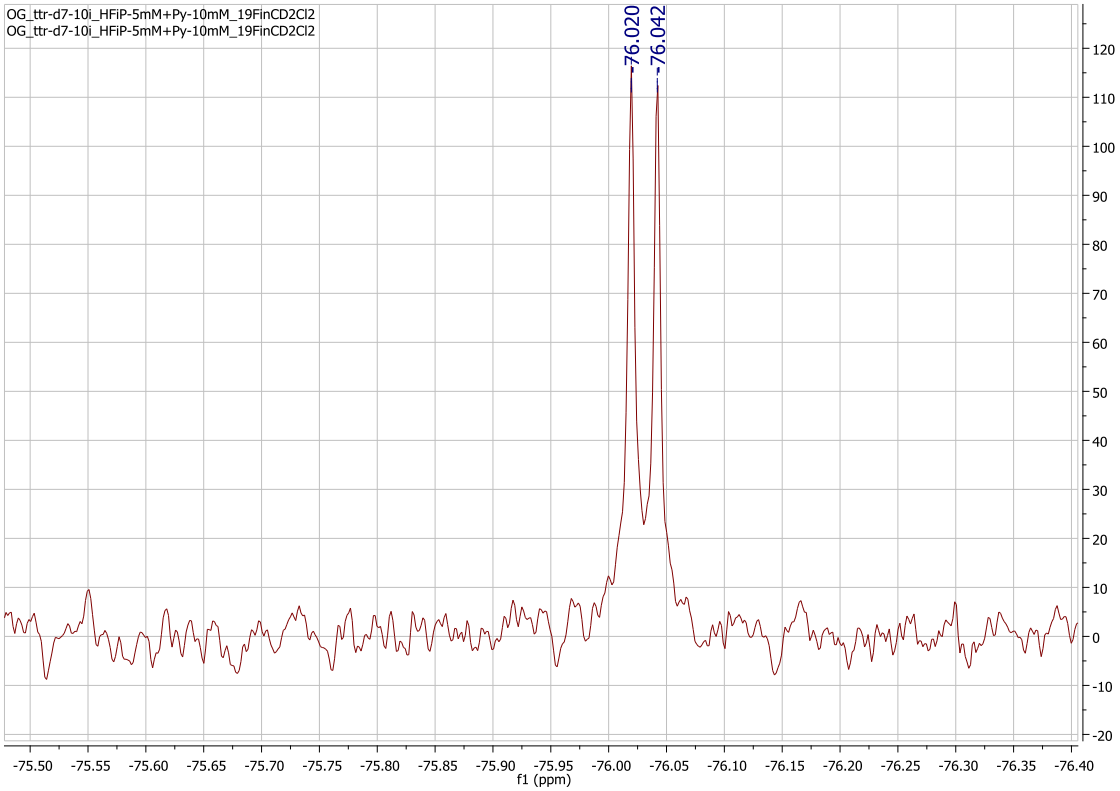

b

Figure s26: Examples of ^{19}F NMR spectra in CD_2Cl_2: 5 mM solution of hexafluoroisopropanol **2** (a); 5 mM solution of hexafluoroisopropanol **2** and 10 mM solution of pyridine **1** (b);

b. Diffusion Coefficients

The diffusion coefficients of pyridine **1**, hexafluoroisopropanol **2**, complex **3**, and dichloromethane-d_2 were determined at 18 °C using diffusion PGSE (Pulsed-field Gradient Spin Echo) NMR experiments (with double-stimulated-echo sequence) and standard fitting techniques (Figures s27-s29).[3] Fitting equation is: $\ln(I/I_0) = -D\gamma^2G^2\delta^2(\Delta-\delta/3)$, where D – diffusion coefficient, I and I_0 – the intensities of a signal in the presence and in the absence of the pulsed-field-gradient, γ – the proton gyromagnetic ratio, G – the pulsed gradient strength, δ – the duration of the pulse, Δ – the time separation between the pulsed-gradients.[3] Water-d_1 (HOD) signal in D_2O was used for the gradient field calibration.[4] The diffusion coefficients of pyridine and hexafluoroisopropanol were determined as 2.95×10^{-9} m^2s^{-1} and 2.68×10^{-9} m^2s^{-1}, respectively, by measurements of 100 mM solutions of one of these reagents in dichloromethane-d_2. The diffusion coefficient of dichloromethane-

d_2 is 3,61 × 10^{-9} m^2s^{-1}, as determined by the measurements of the pure solvent. The diffusion coefficients of complex **3** (pyridine× hexafluoroisopropanol) was determined as 1.91 × 10^{-9} m^2s^{-1} by measurement of a solution containing both 100 mM of pyridine **1** and 100 mM hexafluoroisopropanol **2** in dichloromethane-d_2. It is obtained from the measured value of 2.08 × 10^{-9} m^2s^{-1}, provided that 83.3% of total pyridine exists as the 1:1 complex (based on K_a = 300 M^{-1}). These diffusion coefficient were used as the input data to the COMSOL model.

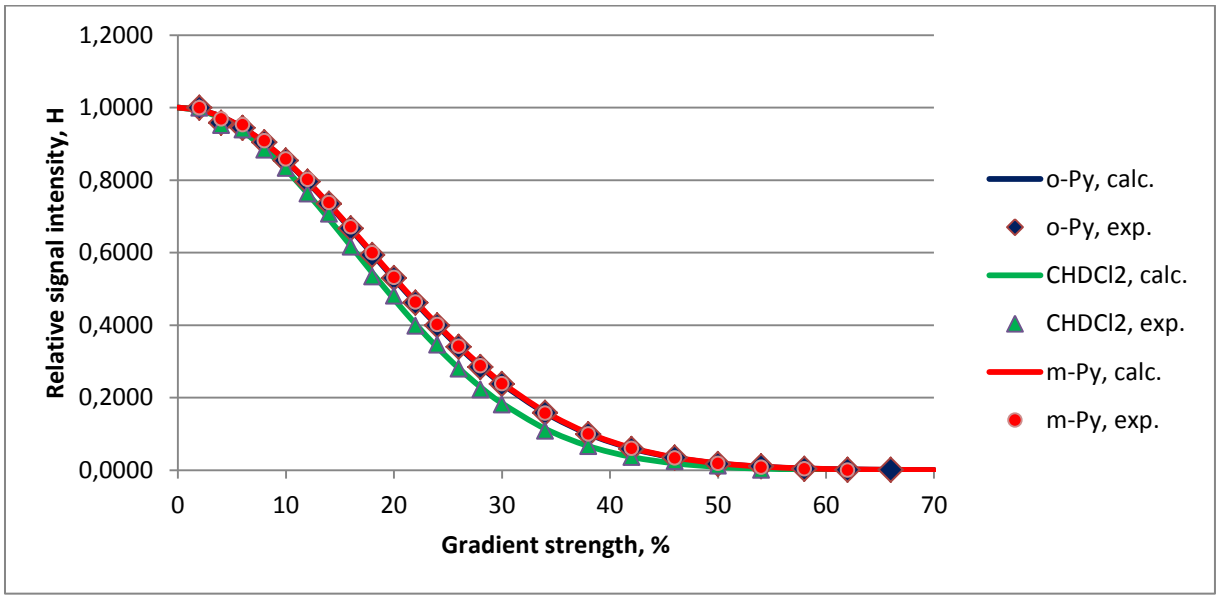

Figure s27. PGSE ^{1}H NMR experiment: 100 mM solution of pyridine **1** in CD_2Cl_2.

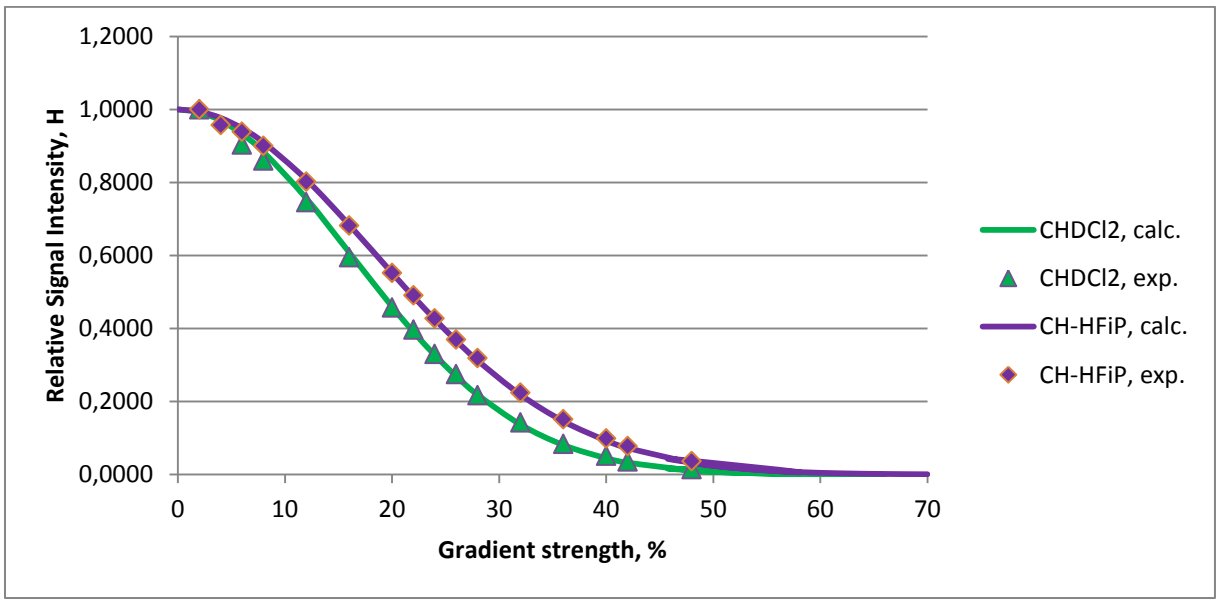

Figure s28. PGSE ^{1}H NMR experiment: 100 mM solution of hexafluoroisopropanol **2** in CD_2Cl_2.

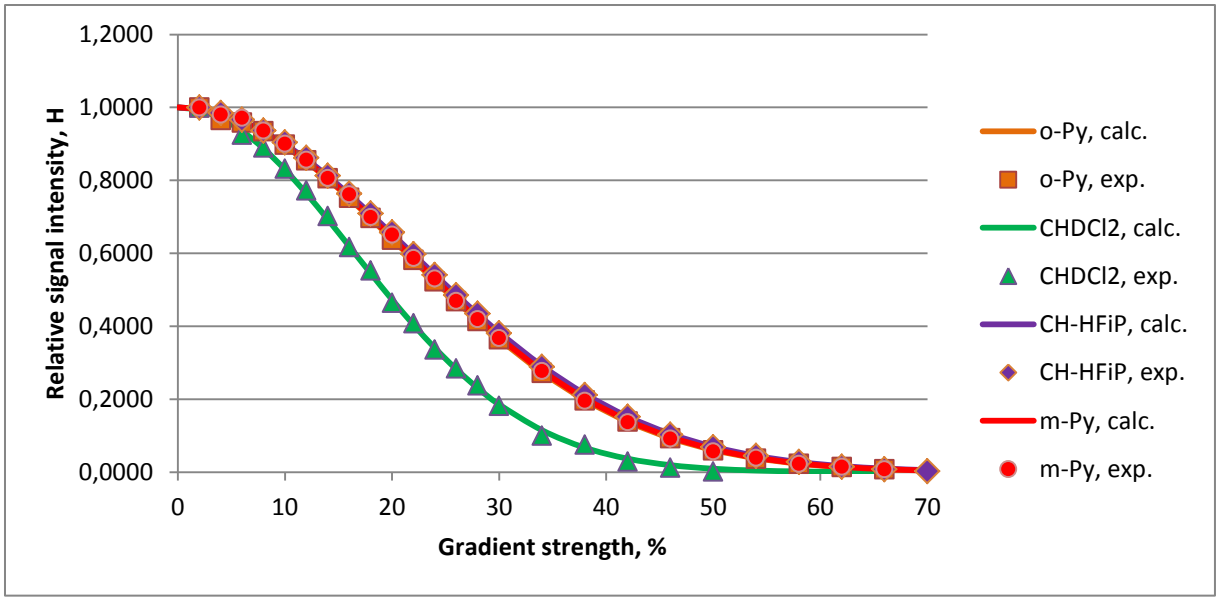

Figure s29. PGSE ^{1}H NMR experiment: 100 mM solution of pyridine **1** and 100 mM solution of hexafluoroisopropanol **2** in CD_2Cl_2.

6. References of the Supporting Information:

(1) Domke, K. F.; Day, J. P. R.; Rago, G.; Riemer, T. A.; Kox, M. H. F.; Weckhuysen, B. M.; Bonn, M. *Angew. Chem., Int. Ed.* **2012**, *51*, 1343; Rago, G.; Langer, C. M.; Brackman, C.; Day, J. P. R.; Domke, K. F.; Raschzok, N.; Schmidt, C.; Sauer, I. M.; Enejder, A.; Mogl, M. T.; Bonn, M. *Biomedical Optics Express* **2011**, *2*, 2470; Day, J. P. R.; Domke, K. F.; Rago, G.; Kano, H.; Hamaguchi, H.-o.; Vartiainen, E. M.; Bonn, M. *J. Phys. Chem. B* **2011**, *115*, 7713; Day, J. P. R.; Rago, G.; Domke, K. F.; Velikov, K. P.; Bonn, M. *J. Am. Chem. Soc.* **2010**, *132*, 8433; Kox, M. H. F.; Domke, K. F.; Day, J. P. R.; Rago, G.; Stavitski, E.; Bonn, M.; Weckhuysen, B. M. *Angew. Chem., Int. Ed.* **2009**, *48*, 8990.

(2) Connors, K. A. *Binding Constants. The measurement of Molecular Complex Stability*; Wiley-Interscience, 1987; Woodbury, C. P. *Introduction to Macromolecular Binding Equilibria*; CRC Press, Taylor & Francis Group, 2008.

(3) Cohen, Y.; Avram, L.; Frish, L. *Angew. Chem., Int. Ed.* **2005**, *44*, 520; Macchioni, A.; Ciancaleoni, G.; Zuccaccia, C.; Zuccaccia, D. *Chem. Soc. Rev.* **2008**, *37*, 479.

(4) R. Mills, *J. Phys. Chem.*, **1973**, *77*, 685